Universitat Autònoma de Barcelona

EFFECT OF FLEXOELECTRICITY ON THE NANO-MECHANICAL PROPERTIES OF FERROELECTRICS

Kumara Cordero - Edwards

ADVERTIMENT. L'accés als continguts d'aquesta tesi queda condicionat a l'acceptació de les condicions d'ús establertes per la següent llicència Creative Commons: http://cat.creativecommons.org/?page_id=184

ADVERTENCIA. El acceso a los contenidos de esta tesis queda condicionado a la aceptación de las condiciones de uso establecidas por la siguiente licencia Creative Commons: http://es.creativecommons.org/blog/licencias/

WARNING. The access to the contents of this doctoral thesis it is limited to the acceptance of the use conditions set by the following Creative Commons license: https://creativecommons.org/licenses/?lang=en

Universitat Autònoma de Barcelona

POSTGRADUATE SCHOOL
PHYSICS DEPARTMENT

Ph. D. THESIS

EFFECT OF FLEXOELECTRICITY ON THE NANO-MECHANICAL PROPERTIES OF FERROELECTRICS

Thesis submitted by
Kumara Cordero - Edwards

to apply for the Degree of Doctor at the
Universitat Autonòma of Barcelona
in the Physics Program

Thesis Advisor: **Gustau Catalan Bernabe**
Thesis co-Advisor: **Neus Domingo Marimon**
Thesis Tutor: **Jordi Sort Viñas**

prepared at Institut de Català de Nanociècia i Nanotecnologìa (ICN2)

defended on:
January 2018

Bellaterra, 15 December de 2017

Prof. Gustau Catalan Bernabe, Profesor ICREA, Dra. Neus Domingo Marimon ambos miembros del grupo **Oxide Nanophysics** en el **Institut Català de Nanociència i Nanotecnologia (ICN2)**, en calidad de directores de tesis y Dr Jordi Sort Viñas, catedrático de la **Universitat Autònoma de Barcelona**, en calidad de tutor de tesis.

CERTIFICAN:

Que Kumara Cordero-Edwards, Bachiller en Física, ha realizado bajo su direccion el trabajo que lleva por titulo***"Effect of flexoelectricity on the nano-mechanical properties of ferroelectrics"***. Dicho trabajo ha sido desarrollado dentro del programa de doctorado de Física y constituye su memoria de tesis doctoral, para optar por al grado de Doctor por la Universitat Autònoma de Barcelona.

Dr. Gustau Catalan Bernabe

Dra. Neus Domingo Marimon

Dr. Jordi Sort Viñas

Resumen

Los materiales ferroeléctricos pueden presentar diversas respuestas electromecánicas. Estas incluyen la electrostricción (deformación proporcional al cuadrado del campo eléctrico) la piezoelectricidad (polarización inducida por una deformación), y la flexoelectricidad, polarización inducida cuando hay un gradiente de deformación. Dado que la flexoelectricidad es proporcional a los gradientes de deformación, y estos, crecen en proporción inversa al tamaño, en la nanoescala la flexoelectricidad puede ser tan o más grande que la piezoelectricidad. La investigación desarrollada en ésta tesis se enfoca en estudiar la interacción entre estas dos propiedades cuando compiten y/o colaboran entre ellas, y específicamente en cómo ésta interacción afecta las propiedades mecánicas de los ferroeléctricos.

Hasta ahora se ha creído que las propiedades mecánicas son invariantes con respecto a al espacio de inversión, es decir que medirlas en una cara o en la opuesta no debería cambiar su valor, incluso cuando el material en cuestión es no-centrosimétrico (piezoeléctrico o ferroeléctrico). Sin embargo, ésta tesis demuestra que, en presencia de gradientes de deformación, la simetría mecánica se rompe: la respuesta mecánica de los ferroeléctricos depende del signo de su polarización. Éste resultado representa un cambio de paradigma y ofrece un nuevo camino para explorar en la física de fractura de sólidos.

Esta tesis está distribuida de la siguiente manera:

El capítulo 1 es una introducción a la física de las propiedades mecánicas, la piezoelectricidad y la flexoelectricidad, mientras que el capítulo 2 describe las técnicas experimentales utilizadas en el proyecto para realizar las medidas de las propiedades mecánicas y electromecánicas.

En el capítulo 3, se describe la caracterización y análisis de las propiedades mecánicas de cristales ferroeléctricos de $LiNbO_3$ con la polarización perpendicular a la superficie, empleando la técnica de nanoindentación. Las propiedades fueron medidas para signos opuestos de polarización, y la inversión de la polarización fue realizada de dos maneras distintas: (1) manualmente, es decir, girando el cristal 180°para acceder a la cara opuesta

del mismo, y (2) utilizando un cristal periódicamente polarizado; en dicho cristal se tuvo por tanto acceso a polarizaciones opuestas desde una misma cara. Se observó que, independientemente del método de inversión, todas las respuestas mecánicas son asimétricas con respecto al espacio de inversión.

En el capítulo 4, a partir de la ecuación de la energía libre de los ferroeléctricos, se desarrolló un modelo capaz de determinar el coeficiente de acoplamiento flexoeléctrico empleando únicamente las medidas mecánicas del material. A partir de éste modelo y los datos obtenidos en el capítulo 3, se obtuvo que el valor de dicho coeficiente para $LiNbO_3$ es f $\sim$ 40 V, un valor más realista que el medido por el método estándar y más cercano al predicho por las teorías de Kogan y Tagantsev.

En el capítulo 5, el objetivo era estudiar el efecto de la flexoelectricidad en la propagación de grietas y la tenacidad de factura en cristales ferroeléctricos con la polarización alineada en el plano. El material utilizado para dicho estudio fue un cristal de $Rb - KTiOPO_4$ con dos dominios antiparalelos en el plano. Mediante indentación, se abrieron grietas paralelas, antiparalelas y perpendiculares a la polarización y se demostró que la propagación de dichas grietas esta intrínsecamente relacionado con la dirección de polarización: la flexoelectricidad disminuye la tenacidad de fractura cuando es paralela a la polarización ferroeléctrica, y por ende las grietas son más largas. Para el concepto de agrietamiento dependiente de la polaridad se acuñó el término “diodo de agrietamiento”.

En el capítulo 6, se plantea una posible aplicación de la asimetría en las propiedades mecánicas reportadas en el capítulo 3: leer el signo de la polarización solamente por medios mecánicos, y de forma no-destructiva. Para demostrar éste nuevo concepto, se utilizó Microscopía de Frecuencia de Resonancia de Contacto en el cristal periódicamente polarizado, obteniendo una lectura en concordancia con los resultados del capítulo 3. Además se mostró que al disminuir el volumen ferroeléctrico, es decir, al trabajar con películas delgadas, la resolución de lectura se ve incrementada considerablemente. Esto demuestra a nivel conceptual que, gracias a la flexoelectricidad, no sólo es posible escribir mecánicamente una memoria ferroeléctrica, sino también leerla.

Finalmente en el capítulo 7 se concluye ésta tesis con un sumario de todos los resultados y sus consecuencias.

Abstract

Ferroelectric materials can present various electromechanical responses. These include electrostriction (strain proportional to the square of the electric field) piezoelectricity (polarization induced by a strain), and flexoelectricity (polarization induced by a strain gradient). Since flexoelectricity is proportional to the strain gradients, and these can grow in inverse proportion to the size, at the nanoscale flexoelectricity can be as big as or greater than piezoelectricity. The research developed in this thesis focuses on studying the interaction between these two properties in ferroelectrics, and specifically on how this interaction affects the mechanical properties of ferroelectrics.

Until now it has been believed that the mechanical properties are invariant with respect to space inversion, that is to say that measuring them on one side or on the opposite side of a crystal should not change their value, even when the material in question is non-centrosymmetric (piezoelectric or ferroelectric). However, this thesis shows that, in the presence of strain gradients, mechanical inversion symmetry breaks down: the mechanical response of ferroelectrics depends not just on the orientation but also on the sign of their polarization. This result represents a paradigm shift in the physics of solid state mechanics and fracture physics, and opens up new and interesting functional concepts such as mechanical reading of polarization.

This thesis is distributed as follows:

Chapter 1 is an introduction to the physics of mechanical properties, piezoelectricity and flexoelectricity, while Chapter 2 describes the experimental techniques used in the project for measuring mechanical and electromechanical properties.

Chapter 3 describes the characterization and analysis of the mechanical properties of $LiNbO_3$ ferroelectric crystals with polarization perpendicular to the surface, using the nanoindentation technique. The properties were measured for opposite polarization signs, and the inversion of the polarization was done in two different ways: (1) manually, that is, turning the crystal 180° to access the opposite side of it, and (2) using a periodically polarized crystal, so that opposite polarizations can be accessed on the same face. It was

observed that, regardless of the “switching” method, all the mechanical responses are asymmetric with respect to space inversion. The causes and consequences of this discovery are discussed.

Chapter 4 derives a free-energy model to quantitatively relate the asymmetry of mechanical responses to the flexocoupling coefficient. Using this model and the experimental results of chapter 3, the flexocoupling coefficient of $LiNbO_3$ was calculated using only the mechanical measurements of the material. The value obtained for $LiNbO_3$ is $f \sim 40$ V. This is a more realistic value than that measured by the standard electromechanical method, and is close to the theoretical value predicted by the theories of Kogan and Tagantsev. The conclusion of this chapter is that mechanical methods not only allow measuring flexocoupling coefficients, but they are quantiatively advantageous when dealing with polar materials where spurious piezoelectricity can artificially enhance the results obtained by conventional electromechanical means.

In Chapter 5, the objective was to study the effect of flexoelectricity on the propagation of cracks and the fracture toughness in ferroelectric crystals with polarization aligned in the plane. The material used for this study was a crystal of $Rb - KTiOPO_4$ (R-KTP) with two antiparallel domains in the plane. Using indentation, sets of cracks were opened in the parallel, antiparallel and perpendicular to the polarization. The results showed unambiguously that the propagation of said cracks is asymmetric and intrinsically related to the direction of polarization: flexoelectricity decreases the fracture tenacity when it is parallel to the ferroelectric polarization, thus yielding longer cracks parallel to the polar direction than antiparallel to it. The term ”cracking diode” was coined to denominate this effect.

Chapter 6 describes the concept demonstration of one possible application of the asymmetry in mechanical properties reported in Chapter 3: read the sign of ferroelectric polarization by purely mechanical means and in a non-destructive way. To demonstrate this new concept, Contact Resonance Frequency Microscopy was used in the periodically poled crystal, obtaining a reading in accordance with the results of chapter 3, namely, that the contact stiffness of down-polarized domains is higher than that of up-polarized domains. It was also shown that, owing to the inverse size dependence of flexoelectricity, working with films results in a considerable resolution increase.. This demonstrates that, by exploiting the interaction between flexoelectricity and ferroelectricity, it is not only possible to mechanically write a ferroelectric memory, but also to mechanically read it.

Finally, in chapter 7 this thesis is concluded with a summary of all the results and their consequences.

Contents

Resumen **i**

Abstract **v**

Table of contents **ix**

List of figures **xi**

I Introduction **1**

1 Introduction **3**
- 1.1 Mechanical properties . . . 4
  - 1.1.1 Elastic properties of material . . . 5
  - 1.1.2 Fracture mechanics of brittle materials . . . 6
- 1.2 Ferroelectric materials . . . 9
- 1.3 Piezoelectricity . . . 11
  - 1.3.1 Historical perspective . . . 11
  - 1.3.2 Basic mathematical formulation . . . 11
- 1.4 Flexoelectricity . . . 14
  - 1.4.1 Historical perspective . . . 14
  - 1.4.2 Basic mathematical formulation . . . 14
  - 1.4.3 Principal characteristics . . . 15

2 Experimental methods **21**
- 2.1 Nanoindentation . . . 22
  - 2.1.1 Description of the technique . . . 22
  - 2.1.2 Oliver - Pharr method . . . 23
  - 2.1.3 Mechanical Energy . . . 26
  - 2.1.4 Indenter geometry . . . 26
  - 2.1.5 Thermal drift corrections . . . 27
- 2.2 Atomic Force Microscopy . . . 27
  - 2.2.1 Operating principle . . . 28
  - 2.2.2 Contact mode . . . 29
  - 2.2.3 Amplitude modulation mode . . . 30
- 2.3 Contact Resonance Frequency . . . 31
- 2.4 Piezoeresponse Force Microscopy . . . 34

2.4.1 Operating principle 34
2.4.2 Vertical and lateral PFM 36
2.4.3 DART PFM 37

II Results and discussion 45

3 Switchable mechanical properties of ferroelectrics 47
3.1 Energy cost of deforming piezoelectric and ferroelectric materials 49
3.1.1 Energy cost under homogeneous deformation 49
3.1.2 Energy cost under inhomogeneous deformation 50
3.2 Free energy of ferroelectric materials 51
3.3 Experiment 53
3.4 Mechanical and flexoelectric properties of LiNbO3 under indentation . . . 55
3.4.1 Indentation measurements on stoichiometric LiNbO3 55
3.4.2 Indentation measurements on congruent LiNbO3 57

4 Nanomechanics: measuring flexoelectricity from nanoindentation 65
4.1 Calculation of the flexoelectric coefficient 66

5 Cracking flexoelectricity 71
5.1 Crack propagation with respect to the polarization 72
5.1.1 Experiment 72
5.2 Crack length behaviour 74
5.3 Mechanical properties behaviour 75
5.4 Domain Switching 78

6 Mechanical reading of polarity 85
6.1 Mechanical stiffness in ferroelectric materials 86
6.2 Mechanical reading of polarization by CRF 86
6.3 Mechanical reading of polarization in thin films: size effect in the mechanical asymmetry 91

III Conclusions 97

7 Conclusions 99

List of Figures

1.1 Typical stress - strain diagram 4
1.2 Crack modes of loading 7
1.3 Ferroelectric hysteresis loop 10
1.4 Scheme of direct and converse piezoelectric effect. 12
1.5 Homogeneous and inhomogeneous defomation scheck 15

2.1 Load-depth indentation curve 23
2.2 Conical indent representation 24
2.3 Types of indentation tips 26
2.4 AFM working principle 28
2.5 Leonard - Jones potential scheme 30
2.6 Contact Resonance Force Microscopy principle 31
2.7 Linear elastic beam model 33
2.8 Vertical and lateral PFM scheme 35
2.9 Schematic illustration of vertical PFM. 36
2.10 Schematic illustration of lateral PFM. 37
2.11 DART principle 38

3.1 Scheme of piezo - flexo interaction 52
3.2 PFM characterization of PPLN 53
3.3 AFM topography of the indented surfaces 54
3.4 Asymmetry behaviuor in SLN 57
3.5 Asymmetry behaviuor in PPLN 59
3.6 3D plot showing showing the switching due to flexoelectric effects 61
3.7 Dielectric characterization of PPLN and SLN 62

5.1 Scheme of the experiment 74
5.2 Crack lenght asymmetry behaviour 75
5.3 Fracture toughness asymmetry behaviour 76
5.4 2D strain field and strain gradien components map arround a crack 81

6.1 Mechancial reading by indentation tests 87
6.2 Mechanical reading on PPLN using CRF, soft tip 89
6.3 Mechanical reading on PPLN using CRF, hard tip 90
6.4 PFM image of switched domains 92
6.5 Mechanical reading in thin films using CRF 93

Part I

Introduction

CHAPTER 1

Introduction

The aim of this thesis is to study how the interplay between piezoelectricity and flexoelectricity affects the mechanical response of ferroelectric materials. Thus, this chapter describes the basic concepts related with mechanical properties, ferroelectric materials, piezoelectricity, and flexoelectricity.

1.1 Mechanical properties

The mechanical properties of materials are those properties that determine the material deformation when a material is subjected to mechanical stresses. Deformation may be elastic (reversible) or plastic (irreversible), with the latter being directly linked to fracture. Mechanical properties determine the stress levels that a material can withstand, to establish the range of uses that it can have and the service life that can be expected; they are, therefore of crucial importance for technological applications. Some of the most important and useful mechanical properties are elasticity, plasticity, ductility, brittleness, stiffness, toughness, hardness, and fracture toughness.

The most elementary, but very important, mechanical property is elasticity.[1] It describes the response of a solid material to a small loading which causes reversible deformations, called elastic deformation. The fundamental material parameters which characterize the elastic behaviour of the solid are the elastic constants. Throughout this thesis the elastic properties will be studied, so this will be explained in details in section 1.1.1

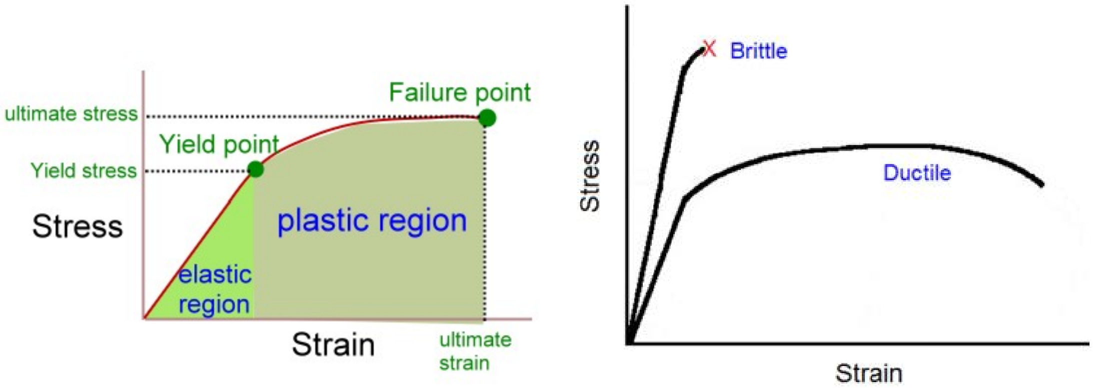

Figure 1.1: *Typical stress – strain diagram showing (a) the elastic region and the plastic region, as well as the elastic limit, the yield stress, and the fracture point, and (b) ductile and brittle material behaviour.*

Conversely, when the loading applied is increased beyond the elastic limit, materials undergo to plastic deformation, which is permanent and irreversible. The stress for which the elastic limit is exceeded and plastic deformation begins is called the yield stress. By applying further loading the material may suffer fracture and break down. A scheme of the elastic and plastic behaviour of materials can be observed in Figure 1.1(a).

Materials characterized as being ductile can suffer large plastic deformations before they finally break, whereas brittle materials, fail at a much earlier stage, as can be observed in Figure 1.1(b). In this thesis, brittle materials (ferroelectric crystals) are studied; therefore the basics of fracture mechanics of brittle materials will be explained in some detail in section 1.1.2.

This thesis focuses on studying the stiffness, hardness, toughness, and fracture toughness on ferroelectric materials. Given that the definition of these properties are often confused, they will be defined below in table **??** in order to clarify they physical meaning.

Parameter	Units	Definition
Stiffness	N/m	The resistance of a material to deflection or deformation.This is also known as the elastic constant, i.e., amount of force required to induce a given deformation.
Hardness	Pa	The ability of a material to resist scratching, indentation, or penetration. Amount of stress at which plastic deformation appears.
Toughness	J/m^3	The ability to absorb energy (plastic and elastic) prior to fracture. Elastic energy density required to induce fracture.
Fracture toughness	$Pam^{1/2}$	The ability of a material containing a crack to resist fracture.Stress intensity required to make a crack propagate.

Table 1.1: *Definition of stiffness, hardness, toughness, and fracture toughness [2-3]*

1.1.1 Elastic properties of material

When a solid body is subject to external forces it is said that the material is in a state of stress. If such forces are applied to the surface of the given part, the force per unit area is called the *stress*. The stress in a crystalline material is a direction dependent quantity and is therefore described by a tensor σ_{ij}.

The deformations of the solid caused by the exerted stress are described by the strain tensor. If *ui* is the displacement of a point xj in a deformed solid, the strain tensor is then defined as

$$\varepsilon_{ij} = \frac{1}{2}\left(\frac{\partial u_i}{\partial x_j} + \frac{\partial u_j}{\partial x_i}\right). \tag{1.1}$$

The diagonal components ε_{11}, ε_{22} and ε_{33} are called tensile strains, whereas the other components are usually denoted as shear strains. In absence of body torques both stress and strain are symmetrical tensors. The most general linear relationship which connects stress to strain is provided by the generalized version of the well-known Hooke's law

$$\sigma_{ij} = C_{ijkl}\varepsilon_{kl}, \tag{1.2}$$

where σ_{ij} denotes the stress tensor, ε_{kl} the strain tensor and the elements of the fourth-order tensor C_{ijkl} are the so-called elastic constants. Alternatively, one might express the strains in terms of the stresses by

$$\varepsilon_{ij} = S_{ijkl}\sigma_{kl} \tag{1.3}$$

defining the elastic moduli S_{ijkl}. The elastic constants and elastic moduli are fundamental materials parameters providing detailed information on the mechanical properties of materials.

1.1.2 Fracture mechanics of brittle materials

Fracture is a process by which the material breaks into two or more parts. In most cases it involves nucleation and a propagation of cracks. There are essentially three basic ways of loading a solid body containing a crack. These are known as loading modes and represent possible symmetric displacements of the upper crack surface against the lower one.

The modes are illustrated in Figure 1.2, the most studied one is the so-called mode I (tensile opening), where the crack faces, under tension, are displaced in a direction normal to the crack plane. The mode I component is prevalent under common tensile loading of the crack. The mode II (shear sliding) and mode III (tearing) loadings represent deformations for which the crack surfaces glide over each other in the same plane, or out of this plane, respectively. There is a difficulty connected with modes II and III, which hampers their experimental surveys. Because the crack faces are not pulled away from one another, the contact between the crack faces is unavoidable and results in friction forces along the crack faces which cause difficulties for the experimental measurements. Therefore, mode I loading is the easiest one to model, and it also corresponds most closely to the conditions implemented in most experimental works. Each of the crack loading modes is associated with a certain stress field in the neighbourhood of the crack. The stress field can be described using the concept of the stress intensity factor K, introduced by Irwin.[5] The general equations that describes the stress field for each crack loading modes are given by[4,6]

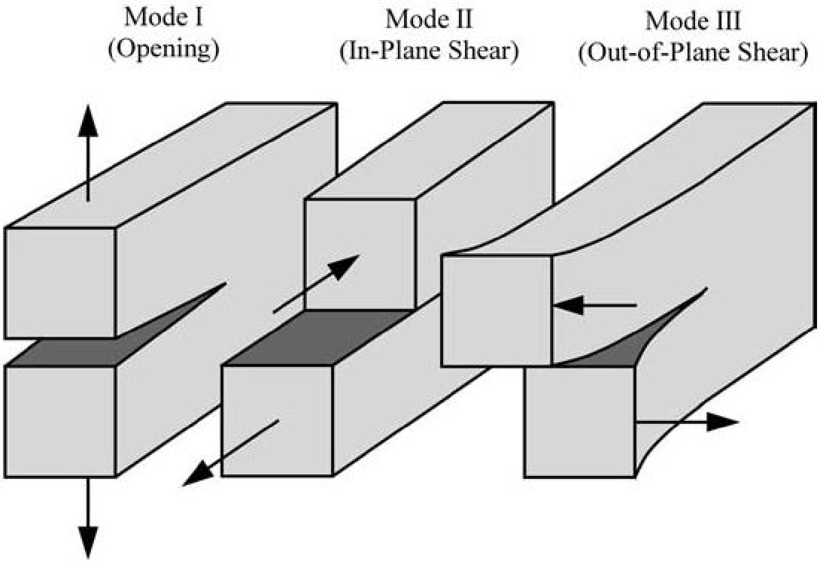

Figure 1.2: *The three modes of loading that can be applied to a crack. Taken from [4]*

$$\sigma_{ij}^{I} = \frac{K_I}{\sqrt{2\pi r}} f_{ij}^{I}(\theta), \tag{1.4}$$

$$\sigma_{ij}^{II} = \frac{K_{II}}{\sqrt{2\pi r}} f_{ij}^{II}(\theta), \tag{1.5}$$

$$\sigma_{ij}^{III} = \frac{K_{III}}{\sqrt{2\pi r}} f_{ij}^{III}(\theta), \tag{1.6}$$

where $f(\theta)$ are universal functions independent of the crack geometry and describe the radial and angular variations of the stresses around the crack. Hence, the local stress field around the crack is fully characterized by the stress intensity factor K, which is related to the applied stress, the crack length and the crack geometry. The stress intensity factor can be expressed in a general form as

$$K = \sigma_a Y \sqrt{\pi c} \tag{1.7}$$

where σ_a is the applied stress, Y is a geometric factor, and c is the crack length. Materials can sustain different critical stresses with a critical value for K associated. This critical stress intensity factor (Kc) is also called fracture toughness.

Griffith [7] found that the critical stress, σ_c, causing the crack to propagate is given by

$$\sigma_c = \sqrt{\frac{2E\gamma}{\pi c}}, \tag{1.8}$$

where E is the elastic modulus and γ is the fracture surface energy. This energy is related with the elastic energy release rate, G, which measures the change of elastic energy per change of crack length. When fracture occurs this energy reaches a critical value, and it is called critical energy release rate G_c. This quantity is in fact a mechanical property, and is related with the fracture toughness by the equation

$$G_c = \frac{K_c^2}{E*} \tag{1.9}$$

where $E*$ is the reduced elastic modulus, the relation of the elastic modulus and the reduced modulus will be explained in section 2.1.

1.2 Ferroelectric materials

Dielectrics can develop a polarization P_i (C/m^2) $(i = 1, 2, 3)$by the influence of an externally applied electric field E_j:

$$P_i = \chi_{ij} E_j, \tag{1.10}$$

where χ_{ij} (F/m) are the components of the dielectric susceptibility tensor. The magnitude of the polarization is defined as the dipole moment per unit volume, which arises as a result of the spatial separation of the centres of positive and negative charges in the molecule or unit cell of the material.

In the case of crystals, the direction of the dipole moment lies along the polar axis, which is usually one of the high symmetry directions of the unit cell.[8] Crystals can be grouped into 7 crystal systems (cubic, tetragonal, orthorhombic, monoclinic, triclinic, hexagonal and trigonal), which are further divided into 32 classes according to theirpoint-group symmetry; 11 of these point groups are centrosymmetric, and the remaining 21 are non-centrosymmetric, because the structure does not possess a center of symmetry, i.e. is not invariant under space inversion. Only 20 of those exhibit piezoelectric effects, and a detailed description of this effect will be in section 1.3. From these 20 classes, polarization can be induced by mechanical stress in 10, while the other 10 possess a spontaneous polarization –they are polar symmetries.

Ferroelectrics materials have a spontaneous electric polarization below a certain phase transition temperature, called Curie temperature. This polarization can be reversed by the application of an external electric field, called coercive field E_c. Depending on the crystalline structure the ferroelectric switching can be of 180°(pure ferroelectric inversion) or of a smaller angle (90°in tetragonal ferroelectrics, or 71°or 109°in rhombohedral ones). A distinctive feature of ferroelectric materials is the emergence of a ferroelectric hysteresis loop as sketched in Figure 1.3.

There is always a spontaneous strain associated with the spontaneous polarization, so any polar switching by an angle smaller than 180°must be associated with a change of

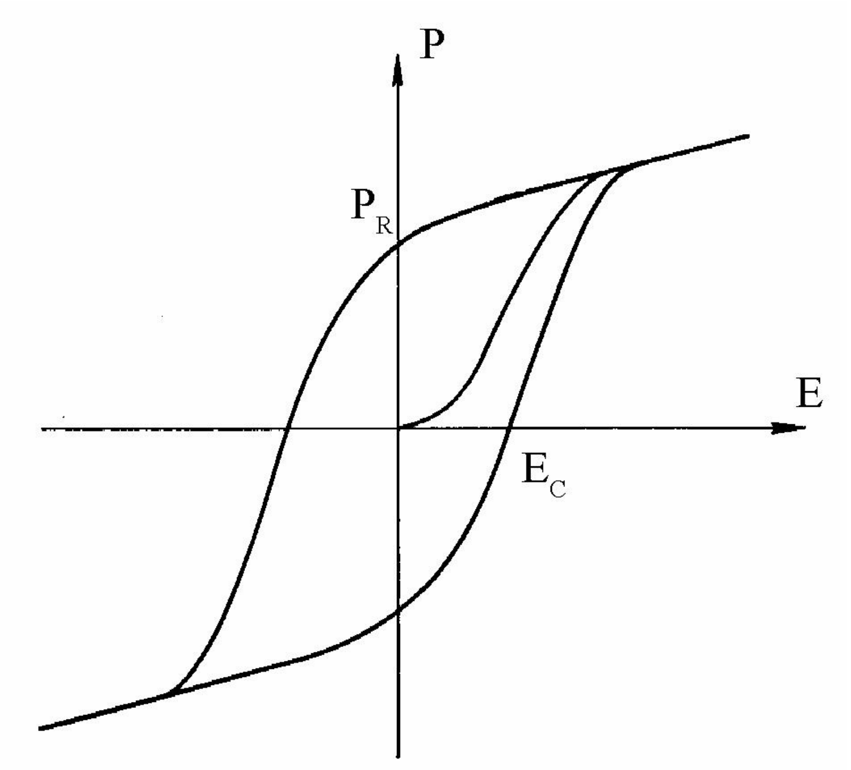

Figure 1.3: *Schematic diagram of a typical ferroelectric hysteresis loop. Taken from [8]*

the spontaneous strain direction, called ferroelastic switching. In contrast, 180°switching does not alter the polar axis, so it does not affect the direction of the spontaneous strain either. In consequence, uniaxial ferroelectric switching is not ferroelastic. Conversely, in a ferroelectric-ferroelastic crystal an external stress may switch the direction of the spontaneous strain and thus change the direction of the ferroelectric axis. Such stress-induced switch is not possible in a uniaxial ferroelectric. The type of ferroelectrics studied in this thesis are the ones in which 180°switching is the only reorientation possibility, i.e. uniaxial ferroelectrics which have only one axis forP_s orientation.

Owing to their switchable spontaneous polarization, the polarization-strain coupling, and their very high dielectric constant, ferroelectric materials have a wide range of technological applications.[9-13] In all these applications, ferroelectrics may experience deformations due to mechanical stress or the application of an electric field, so the crucial role of the mechanical and electromechanical properties of these materials is obvious.

This thesis studies the mechanical properties and the mechanical response of ferroelectrics, taking into account two electromechanical responses: piezoelectricity, explained in section 1.3, and flexoelectricity, explained in section 1.4.

1.3 Piezoelectricity

1.3.1 Historical perspective

Etimologically the word piezoelectricity can be separated into two Greek roots: *piezein* that means to press or to squeeze, and *elektron* meaning amber, describing substances that (like amber) attract other substances when rubber. Piezoelectricity thus literally means pressure induced electricity.

This phenomenon was discovered by Jacques Curie and Pierre Curie in 1880, when they observed that pressing in a certain direction on crystals of tourmaline, quartz, can sugar and Rochelle salt, these crystals were able to generate change on certain positions of their surfaces, i.e. they observed electrification under mechanical pressure.[14] The following year, Lippman,[15] from thermodynamic considerations, predicted the converse effect: an imposed voltage produces mechanical deformations or strains the material; which was experimentally verified by Curie brothers in the same year.[16]

1.3.2 Basic mathematical formulation

The direct piezoelectric effect can be represented by the equation:

$$P_i = d_{ijk}\sigma_{jk} \tag{1.11}$$

where P_i is the polarization vector (C/m^2), d_{ijk} is the third rank tensor of direct piezoelectric coefficients (C/N), and σ_{jk} is the second-rank stress tensor (Pa). The subscripts can take vales 1, 2, 3 representing the tree orthogonal directions. The polarization involves one direction, i the polar axis, and the stress two directions, j is the direction of the force and k is the normal to the face it acts on. Therefore, the piezoelectric coefficient must involve three directions to relate those two quantities.[17]

Inversely, the converse piezoelectric effect describes the changes in dimensions of a piezoelectric material in response to an applied electric field E, which can be mathematically represented as follow:

$$\varepsilon_{jk} = d_{ijk} E_k \tag{1.12}$$

where ε_{jk} is the second rank strain tensor, which is dimensionless, d_{ijk} is the third rank tensor of the converse piezoelectric coefficients (m/V), and E_i is the electric field vector (V/m). Figure 1.4 shows a sketch of both direct and converse piezoelectric effect.

The coefficients connecting the field and strain in the converse effect are the same as those connecting the stress and the polarization in the direct effect. The proof of this equality is based on the thermodynamic reasoning that both piezoelectric effects can be obtained by the differentiation of the same Gibbs free energy to both stress and electric field. [18] In general, the piezoelectric third rank tensor has 27 components, but due to the symmetry of the stress (strain) tensor which allow for the contraction of the stress (strain), the piezoelectric tensor can be also contracted, thus the ij indices of d_{ijk} is contracted exactly as the indices of the stress (strain) tensor, therefore only 18 of those components are independent.[17] The notation of equations 1.11 and 1.12 can be simplified using matrix

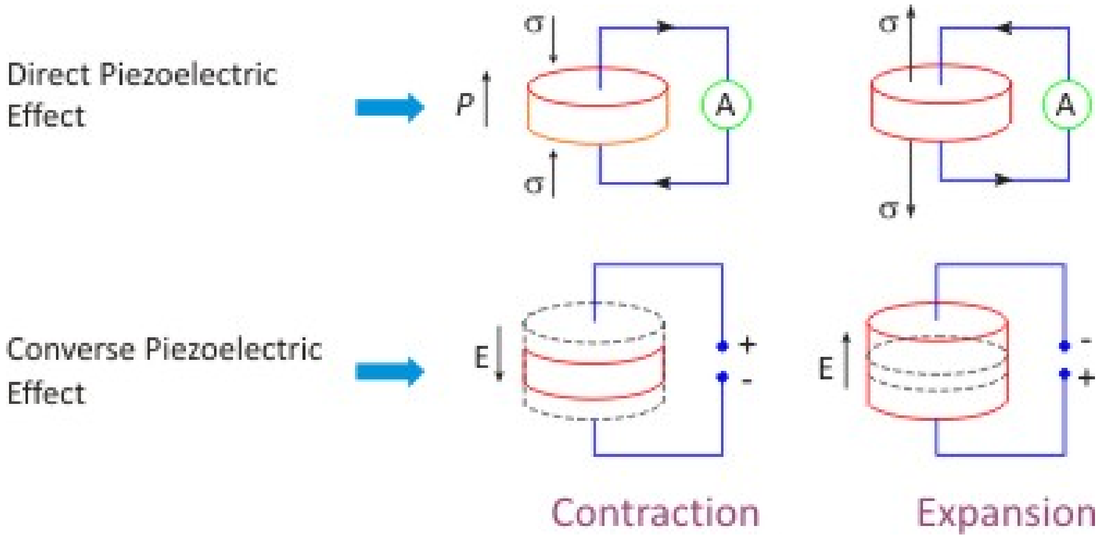

Figure 1.4: *Scheme of direct and converse piezoelectric effect.*

notation and Voigt convention: a pair of indices $ii = 11$, 22, 33 can be written as $m = 1$, 2, 3, respectively, and the mixed pairs of indices (which represent shear components of strain and stress tensors) $ij = 23$ or 32, 13 or 31, 12 or 21 as $m = 4$, 5, 6, respectively.[18] The direct piezoelectric equation rewrite in matrix notation is the following

$$\begin{pmatrix} P_1 \\ P_2 \\ P_3 \end{pmatrix} = \begin{pmatrix} d_{11} & d_{12} & d_{13} & d_{14} & d_{15} & d_{16} \\ d_{21} & d_{22} & d_{23} & d_{24} & d_{25} & d_{26} \\ d_{31} & d_{32} & d_{33} & d_{34} & d_{35} & d_{36} \end{pmatrix} \begin{pmatrix} \sigma_1 \\ \sigma_2 \\ \sigma_3 \\ \sigma_4 \\ \sigma_5 \\ \sigma_6 \end{pmatrix} \tag{1.13}$$

and the inverse piezoelectric equation as

$$\begin{pmatrix} \varepsilon_1 \\ \varepsilon_2 \\ \varepsilon_3 \\ \varepsilon_4 \\ \varepsilon_5 \\ \varepsilon_6 \end{pmatrix} = \begin{pmatrix} d_{11} & d_{12} & d_{13} & d_{14} & d_{15} & d_{16} \\ d_{21} & d_{22} & d_{23} & d_{24} & d_{25} & d_{26} \\ d_{31} & d_{32} & d_{33} & d_{34} & d_{35} & d_{36} \end{pmatrix} \begin{pmatrix} E_1 \\ E_2 \\ E_3 \end{pmatrix} \tag{1.14}$$

Commonly the coefficient measured in the direction of the applied field is called longitudinal coefficient whereas the one measured perpendicular to the field is the transverse coefficient and the others the shear coefficients. A number of techniques have been developed to measure piezoelectric coefficients through the direct and converse piezoelectric effect. One of those using the converse piezoelectricity is PFM, explained in details in section 2.4, which allows to measure the d_{33} and d_{15} coefficients.

The reason there is a detailed discussion of piezoelectricity and its symmetry in this section is that the competition between piezoelectricity and flexoelectricity, and their different symmetry restrictions, is vital to explain the new physical phenomena described in chapters 3-6 of this Thesis.

1.4 Flexoelectricity

1.4.1 Historical perspective

Flexoelectricity is defined as the linear coupling between polarization and strain gradients, and has drawn scientific interest since it was first introduced more than fifty years ago. In the early 60s, Mashkevich and Tolpygo[19] proposed a new phenomenon that linked electrical polarization with inhomogeneous deformation. The theoretical framework was developed by Kogan [20] in 1964, who predicted the flexoelectric coefficient to have an order of magnitude$\sim e/a$, where e is the electron charge and a is the lattice constant. The converse phenomenon of strain gradient induced by polarization was described in 1968 by Bursian [21], who also demonstrated that it was proportional to the dielectric susceptibility [22]. In 1981 Indenbom[23] named this phenomenon as flexoelectricity, and in 1986, Tagantsev[24] developed a more detailed phenomenological theory of flexoelectricity, demonstrating that in materials with high dielectric susceptibility this effect must be enhanced. This enhancement in the flexoelectric effect has been experimentally verified in materials such as relaxors ferroelectrics,[25-26] ferroelectric ceramics,[27, 28, 29] and ferroelectric single crystals.[30-31] The current experimental and theoretical state of the art has been summarized in different reviews.[32-35]

1.4.2 Basic mathematical formulation

The direct flexoelectric effect describes the generation of an electric polarization response under a mechanical strain gradient, and mathematically it is described by:

$$P_i = \mu_{ijkl} \frac{\partial \varepsilon_{kl}}{\partial x_j}, \tag{1.15}$$

where μ_{ijkl} is the flexoelectric coefficient, a fourth rank tensor that relates the induced polarization P_i with the strain gradient $\frac{\partial \varepsilon_{kl}}{\partial x_j}$, a third rank tensor. Meanwhile, the converse flexoelectric effect describes the mechanical stress induced by an electric field gradient, and it is given by

$$\sigma_{kl} = \mu_{ijkl} \frac{\partial E_i}{\partial x_j}. \tag{1.16}$$

1.4.3 Principal characteristics

Unlike piezoelectricity, this property is allowed in all dielectric materials regardless of their symmetry. This is a direct mathematical consequence of the fact that, unlike the piezoelectric tensor, the flexoelectric tensor is of even parity, but Figure 1.5 explains more intuitively the reason of this universality: When a centrosymmetric unit cell is subjected to a homogeneous deformation all the ions move in the same way, preserving the centre of inversion, thus a null polarization is achieved. In contrast, when the deformation is inhomogeneous the centre of the positive and negative charges are separated and a dipole is formed, thus a polarization is achieved. Despite being a universal property, flexoelectricity has received less attention than piezoelectricity, because at macroscopic scales the amount of bending that can be induced is generally small and therefore its effects are weak. However, flexoelectricity has a unique intrinsic effect, related to the fact that strain gradients are size-dependent property that scales in inverse proportion to size, therefore flexoelectricity can be huge at the nanoscale. An inctuitive way to understand this is that the strain gradient is measured as the inverse of the radius of curvature, and

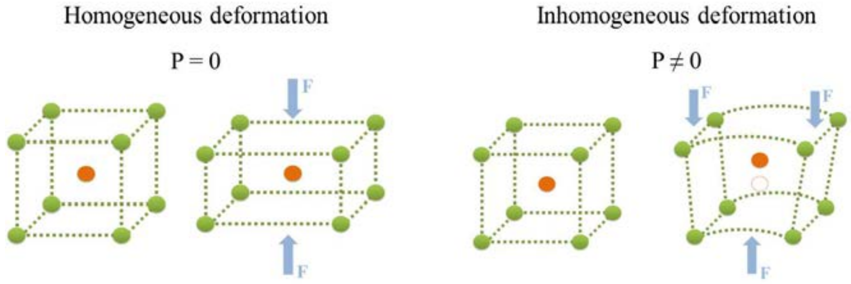

Figure 1.5: *Scheck of a cubic unit cell under homogeneous and inhomogeneous deformation.*

this radius of curvature can never be smaller than the thickness of the bent sample.

Another factor that has increased the interest in flexoelectricity is that, as mentioned above, it scales with the dielectric constant, so it can be large in high-permittivity materials such as ferroelectrics but also of non-ferroelectric oxides such as $SrTiO_3$. Due to this, flexoelectricity has been thought of as a substitute for piezoelectricity; however, throughout this thesis it will be demonstrated that it is often more interesting to examine the coexistence of both, since their interaction gives rise to new physics.

References

1. Timoshenko, S. & Goodier, J.N. *Theory of elasticity.* 3rd Edition, McGraw Hill Press (1951).
2. Tabor, D. *The Hardness of Metals.* Clarendon Press Oxford (1951).
3. François, D., Pineau, A. & Zaoui, A. *Mechanical Behaviour of Materials.* 2nd Edition, Springer Press (2012).
4. Anderson, T.L. *Fracture mechanics: fundamentals and applications.* 3rd Edition, CRC Press (2005).
5. Irwin, G. R. *J. Appl. Mech.* **24**, 361 - 364 (1957).
6. Lawn, B. *Fracture of brittle solids.* 2nd Edition, Cambridge University Press (1993).
7. Griffith, A.A. *Philos. Trans. R. Soc. London Ser.* **A221**, 163–198 (1920).
8. Jona, F. & Shirane, G. *Ferroelectrics cystals.* Clarendon Press (1962).
9. Scott, J. F. & Paz de Araujo, C.A. *Science* **246**, 1400 – 1405 (1989).
10. Park, S. E. & Shrout, T. R. *J. Appl. Phys.* **82**, 1804 – 1811 (1997).
11. Ahn, C.H., Rabe, K.M., Triscone, J.-M. *Science* **303**, 488-491 (2004).
12. J. F. Scott. *Science* **315**, 954-959 (2007).
13. Qi, Y., Jafferis, T., Lyons, K., Lee, C. M., Ahmad, H.& McAlpine, M. C. *Nano. Lett.* **10**, 524 – 528 (2010).
14. Curie, P. & Curie, J. C. *R. Acad. Sci.* **91**, 294 – 295 (1880).
15. Lippmann, G. *Ann. Chim. Phys.* **24(5a)**, 145 – 178 (1881).
16. Curie, P. & Curie, J. C. *R. Acad. Sci.* **93**, 1137 – 1140 (1881).

17. Newnham, R.E. *Properties of materials.* Oxford University Press (2005).

18. Damjanovic, D. *Rep. Progr. Phys.* **61**, 1267 – 1324 (1998).

19. Mashkevich, V.S. & Tolpygo, K. B. *Zh. Eksp. Teor. Fiz.* **31**, 520 (1957); *Sov. Phys. JETP* **4**, 1297 (1957).

20. Kogan, S. M. *Sov. Phys. Solid State* **5**, 2069 (1964).

21. Bursian, E. V. & Zaikovkii, O. I *Fiz. Tverd. Tela* **10**, 1413 (1968); [*Sov. Phys.-Solid State* **10**, 1121 (1968)]

22. Bursian. E. V. & Trunov, NN. *Sov. Phys. Solid State* **10**:760–62 (1974).

23. Indenbom, V. L., Loginov, E. B. & Osipov, M. A. *Kristalografija* **26**, 1157 (1981).

24. Tagantsev, A. K. *Phys. Rev. B* **34**, 5883 (1986).

25. Ma. W & Cross. L. E. *Appl.Phys. Lett.* **78**, 2920 (2001).

26. Narvaez, J. & Catalan, G. *Appl. Phys. Lett.* **104**, 162903 (2014).

27. Ma, W. and Cross, L. E. *Appl. Phys. Lett.* **81**, 3440 (2002).

28. Ma, W. and Cross, L. E. *Appl. Phys. Lett.* **82**, 3293 (2002).

29. Ma, W. and Cross, L. E. *Appl. Phys. Lett.* **88**, 232902 (2006).

30. Zubko, P., Catalan, G., Buckley, A., Welche, P.& Scott, *J. Phys. Rev. Lett.* **99**, 167601, (2007).

31. Narvaez, J., Saremi S., Hong, J., Stengel, M. & Catalan, G. *Phys. Rev. Lett.* **115**, 037601 (2015).

32. Cross, L. E. *J. Mat. Sci.* **41**, 53 (2006).

33. Zubko, P., Catalán G. & Tagantsev. A.K. *Annu. Rev. Mater. Res.* **43**, 387 – 421 (2013).

34. Yudin P. V.& Tagantsev. A.K. *Nanotech.* **24**, 432001 (2013).

35. Nguyen, T. D., Mao, S., Yeh, Y. W., Purohit P. K. & McAlpine, M. C *Adv. Mater.* **25**, 946–974 (2013).

CHAPTER 2

Experimental methods

This thesis focuses on the study of the interplay between piezoelectricity and flexoelectricity in ferroelectric materials. Specifically on how cooperation and competition between them affects the mechanical properties and/or mechanical response of these materials. The present chapter describes the main experimental techniques employed to investigate these electro-mechanical phenomena The mechanical properties and mechanical energy were measured by Nanoindentation. Piezoelectric Force Microscopy was used to image the electromechanical response and determine the polarity of ferroelectric domains, while and Contact Resonance Force microscopy was used to map and measure the mechanical response contrast at the nanoscale.

2.1 Nanoindentation

In 1822 Mohs [1] established a technique to measure the hardness of a material by ranking its ability to scratch or be scratched by another material and a maximum value of 10 was assigned to diamond. This technique was the first documented hardness test, and gave rise to techniques used nowadays, known as indentation.

Indentation testing is a simple and convenient way to measure the mechanical properties of a material. This technique consists essentially of pushing an indenter tip into a material and measuring the load and displacement at the tip in order to determine mechanical properties of the sample. The most common properties measured are hardness and elastic modulus, which can be calculated using an appropriate contact mechanics model, and the tip – sample contact area. Instrumentation has evolved towards miniaturization in the last two decades, and is now capable of probing at the nanometre scale. Among those a relevant technique for characterising mechanical behaviour with a few nanometres resolution has emerged, named nanoindentation.

2.1.1 Description of the technique

Nanoindentation test allow extracting the elastic modulus (E) and hardness (H) of a material from a load – displacement measurements. These measurements consist in the application of a controlled load (in μN-mN range), and the detection of the induced depth (in nm-μm range) of the material deformation under a hard indenter tip, typically made of diamond. An archetypal load-displacement curve is shown in Figure 2.1.

The loading portion of the curve incorporates the convoluted response of the material to strain including elastic and plastic deformation mechanisms. However, the unloading portion of the curve, for most materials, consists mainly of elastic recovery.

Methods for determining the mechanical properties of a material are derived from classic contact mechanics equations, such as the Hertz model which deals with the elastic contact between two materials [2], and the relationship between the load, depth, and

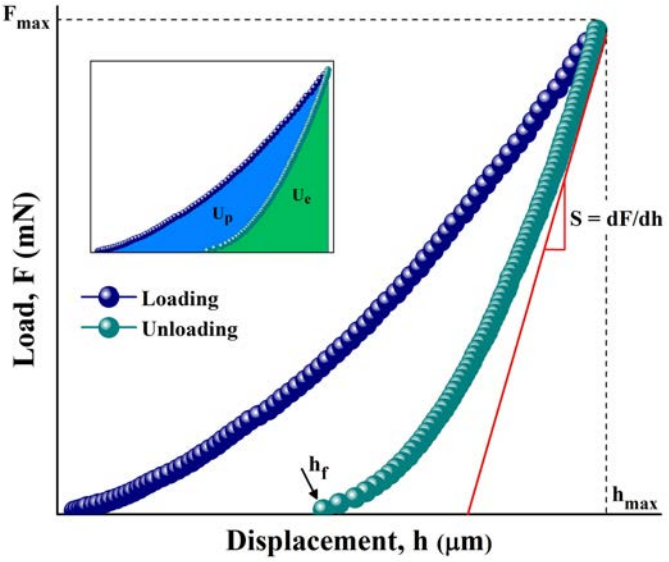

Figure 2.1: *Typical load – depth curve from an indentation.*

contact area derived in 1965 by Sneddon [3]. In the earlies 90's this model was expanded by Oliver and Pharr [4], and has becomes as one of the most common and accurate methods to extract the mechanical properties of materials at the nanoscale. Precisely, the Oliver – Pharr method is used throughout this thesis to determine the energy cost and mechanical properties from the indentation data.

2.1.2 Oliver - Pharr method

In 1992, Oliver and Pharr popularized nanoindentation as a technique to extract elastic properties for materials. This method is based on the following assumptions:

1. the specimen is an infinite half-space.

2. the indenter has an ideal geometry.

3. the material is linearly elastic and incompressible.

4. there are no interaction surface forces during contact such as adhesive or frictional forces.

Oliver and Pharr determined that the unloading curve follows a power law relation

$$P = \alpha(h - h_f)^m, \tag{2.1}$$

where α and m are power law fitting constants. [4] The derivative of equation 2.1 becomes as the stiffness of the elastic contact (S) evaluated at the peak load, Fmax, and peak depth, hmax, i.e. the slope of the upper portion of the unloading curve during the initial stages of unloading, as can be seen in Figure 2.1.

The procedure used to measure H and E is also based on the unloading processes shown schematically in Figure 2.2 The behaviour of the indenter can be modelled by a conical indenter with a half-included angle, ϕ. Assuming that pile-up is negligible, the elastic models show that the amount of sink-in, hs, is given by

$$h_s = \epsilon \frac{P_{max}}{S}, \tag{2.2}$$

where ϵ is a constant that depends on the geometry of the indenter, named intercepted factor. Pharr and Bolshakov [5] proposed a method to determine the values of this constant. Values of ϵ, for commonly used indenter shapes, are provided in Table 2.1 in § 2.1.5. By subtracting the surface displacement (equation 2.2) from the maximum displacement,

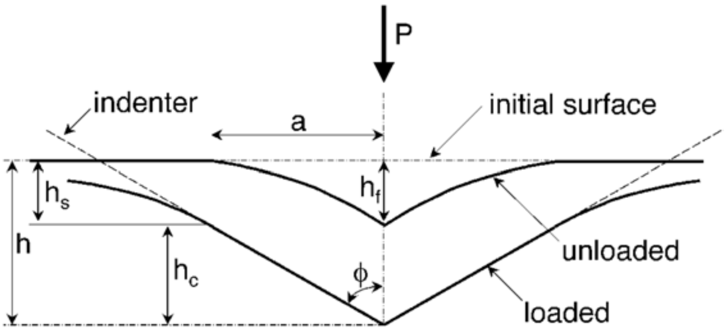

Figure 2.2: *Schematic representation of a section through the peak of a conical indent with relevant quantities labelled. Taken from [6].*

hmax, the depth of the contact impression, hc, is obtained using the following equation:

$$h_c = h_{max} - h_s. \tag{2.3}$$

The contact area is defined by the indenter geometry as

$$A = f(h_c), \tag{2.4}$$

where f is a function relating the penetration depth to the projected contact area of the indenter. This projected contact area is the cross sectional area of the indenter at the depth of interest. This is used, instead of the surface area in contact with the material, because it has a physical relationship to the stress applied to the sample. From the contact area determined, the hardness is estimated from

$$H = \frac{P_{max}}{A}. \tag{2.5}$$

Determining the elastic modulus of the sample requires another extra consideration. The indenter tip, preferably made of diamond, is not perfectly rigid, therefore it elastically deforms simultaneously with the sample, so this must be taken into account, using the expression for the reduced Young's modulus given by

$$\frac{1}{E_r} = \frac{1-\nu^2}{E} + \frac{1-\nu_i^2}{E_i}, \tag{2.6}$$

where ν is the Poisson's ratio and E is the Young's modulus of the specimen, and ν_i is the Poisson's ratio and E_i is the Young's modulus of the indenter. This reduced modulus can be determined from the sample stiffness and the contact area, using

$$E_r = \frac{\sqrt{\pi}}{2\beta}\frac{S}{\sqrt{A}}. \tag{2.7}$$

Here another correction factor, β, is introduced. This factor addresses the axial variation in stress introduced by non-axisymmetric, polygonal, indenter shapes. There has been intense debate over the values of β [4,6]. Values of β, for commonly used indenters can be found in Table 2.1 in § 2.1.4.

2.1.3 Mechanical Energy

In addition to H, E_r, and S, it is possible to obtain the energy involved in the indentation process from the curve load displacement. In general, the indentation process consists of an elastic – plastic deformation (loading) followed by an elastic recovery (unloading) in which the load F and the depth penetration h are related. Therefore, as can be seen in the inset of Figure 2.1, the area under the unloading curve represents the energy recovered (i.e. elastic energy), U_e; whereas the area enclosed between the load and the unload nanoindentation curves represents the energy loss due to plastic deformation U_p. The sum of the elastic energy and plastic energy represents the total work of indentation U_t.

2.1.4 Indenter geometry

There are several different indenter geometries in common usage. Some of these, such as the Brinell sphere, Rockwell conospheroids, and Vickers and Knoop pyramids, are mostly used for macro-micro scale indentation. While others like Berkovich and cube corner indenters are uniquely suited to nano-scale testing. Figure 2.3 shows the schematic shape of these indentation geometries. Regardless the scale on which they are used, each of these

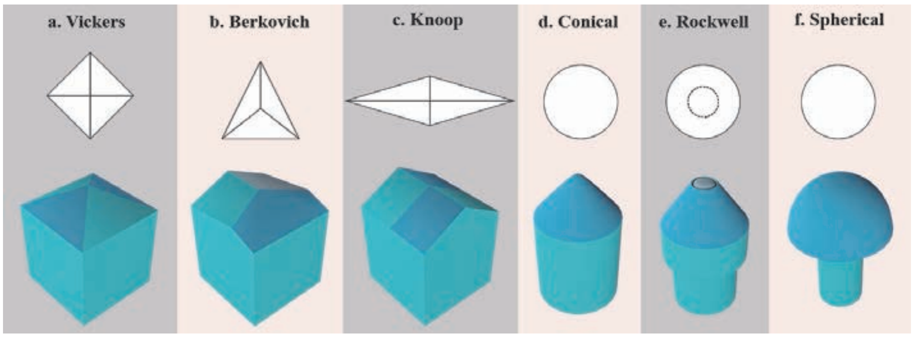

Figure 2.3: *Schematic view of (a) Vickers, (b) Berkovich, (c) Knoop, (d) Conical, (e) Rockwell, and (f) Spherical indenter geometries with the corresponding print.*

geometries has its own intercepted factor (ϵ), correction factor (β), and projected area; all of them critical to quantitatively determine the value of the mechanical properties. Table 2.1 shows the parameters for most common indenter shapes.

In this thesis the indenter geometries used were Berkovich and Vickers.

2.1.5 Thermal drift corrections

Thermal drift, expressed as nm/s, is related to the variations in the measured depth resulting from thermal expansion or contraction of the sample or the indenter during an indentation test. These variations can be minimised by placing the system in a thermally controlled chamber or waiting until thermal equilibrium is established before beginning of the test.

However experimental measurement of the drift rate during each indentation should be made for accurate work. This is done by indenting the specimen with a known constant force and monitoring the displacement signal. If the thermal drift rate is a constant, then it is possible to correct experimental data by the drift rate to compensate. In the experiments shown in this thesis thermal drift corrections were made and it was always kept below ± 0.05 nm/s.

2.2 Atomic Force Microscopy

The invention of the Scanning Tunneling Microscope (STM) in 1981[10] triggered the development of a family of new microscopes, nowadays referred to as Scanning Probe Microscopy (SPM). Currently one of the most broadly employed tool of the SPM family is the Atomic Force Microscopy (AFM), which was invented in 1986 by Binning, Quate, and Gerber.[11]

In standard AFM, a sharp probe (tip) is attached to the end of a flexible cantilever. The force interaction between the probe and the sample surface is utilized to generate a topographical image of the sample surface with atomic resolution.[12, 13, 14, 15] This resolution dependent on the sharpness of the probe in addition to experimental settings (imaging mode of use, imaging environment, flatness of sample, noise levels etc.) but typically for environmental AFMs it is possible to achieve a lateral resolution of ~ 1-10 nm and vertical resolution of < 0.1 nm.

AFM is a unique tool in material science because, in addition to topographic information, it can be used to measure a wide range of surface properties, such as adhesion, friction, electric, magnetic, mechanic, chemical, and elastic, to name a few. Moreover, the measurements can be performed on any kind of material, and in a wide variety of environmental conditions.

2.2.1 Operating principle

The operational scheme of an AFM is shown in the Figure 2.4 The main components of an AFM are a) the cantilever with a tip at the end, which is used as sensor, i.e. a MEMS (micro – electro – mechanical system); b) the laser, photodetector or photodiode, which are used to detect the movement of the cantilever; and c) the scanning system, which is composed by x – y – z scanners generally made by piezoelectric elements, and the controller and feedback electronics.

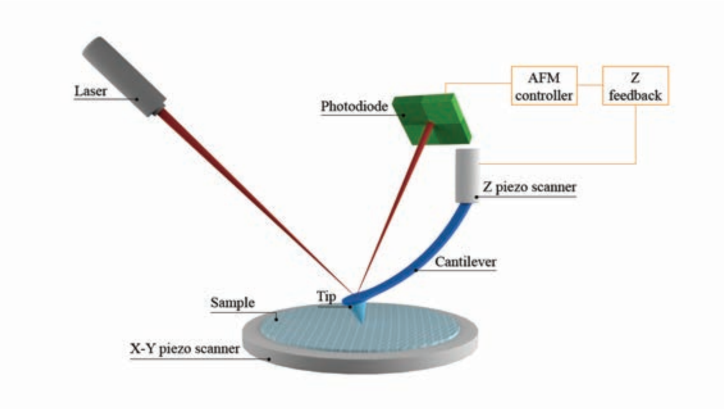

Figure 2.4: *Scheme of an AFM work principle in which are shown all the operational components.*

The way these components work is as follows: the laser beam is focused on top of the back of the free end of the cantilever and reflected onto the photodiode, which is divided in four quadrants, allowing the detection of longitudinal bending and lateral torsion of the cantilever. Before start imaging, the laser reflection is aligned with respect to the photodiode, in such a way that it is centred in the photodiode (as can be seen in Figure 2.4). As the tip is brought close to surface, the cantilever reacts to the forces between the tip and the surface, deflecting in first approximation according to Hooke's law. Many kinds of atomic forces are involved in such interaction, among which the van der Waals force is the dominant one.

By scanning the tip across a surface the cantilever reacts to the topography of the sample, and its movement is collected by the photodiode, which transforms the optical signal in electrical signal. This signal is coupled into feedback electronics that automatically adjusts scanning parameters in order to keep the imaging mode dependent feedback signal constant.

There are two main operational modes in AFM contact mode [11] in which the cantilever is used as a deflection based force sensor, and dynamic mode for which the cantilever is used as a resonator. Dynamic modes are divided in Amplitude modulation (AM – AFM)[16 - 17] and Frequency modulation (FM – AFM)[18] depending on which are the controlled magnitudes of the resonator.

2.2.2 Contact mode

Contact mode was the first and most basic AFM mode developed. In this mode the tip is gently touching the sample. When the tip is brought into close proximity to the sample surface, the cantilever bends due to repulsive interactions, as shown in the Figure 2.5, following Hooke's law

$$F = -k\Delta z \tag{2.8}$$

where k is the spring constant of the cantilever, Δz is the bending of the cantilever, and F is the force exerted on the sample. For small Δz, the displacement can be approached by the angular deflection of the cantilever, which is used as a feedback parameter to keep the tip – sample force interaction constant.

Scanning over the surface features causes the cantilever deflection to change. The feedback loop (in this case the deflection of the cantilever) regulates the vertical Z scanner position in a way to maintain the deflection constant to the setpoint and so the force topography image is obtained as the recorded z – scan movement.

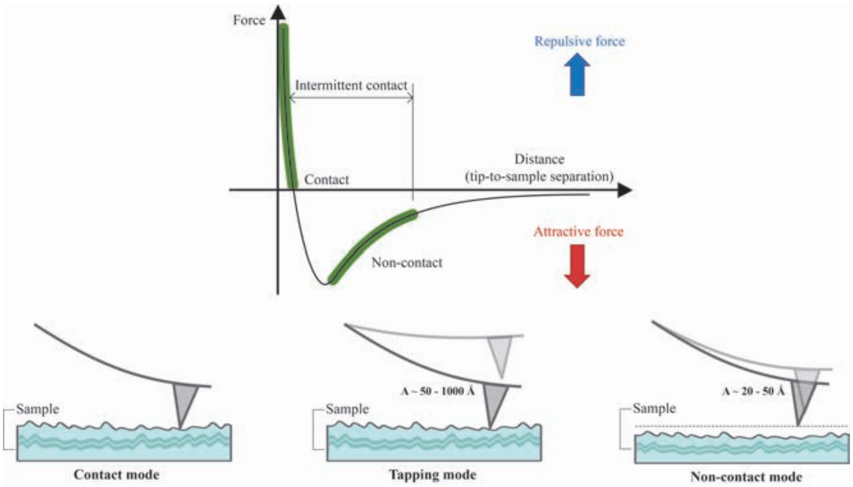
Force
Repulsive force
Intermittent contact
Distance
(tip-to-sample separation)
Contact
Attractive force
Non-contact
Sample
Contact mode
A ~ 50 - 1000 Å
Sample
Tapping mode
A ~ 20 - 50 Å
Sample
Non-contact mode

Figure 2.5: *Scheme of tip-sample interaction described by the Leonard – Jones potential.*

Contact mode is predominately used in this thesis, since is the base of CRFM (explained in § 2.3) and PFM (explained in § 2.4) imaging modes.

2.2.3 Amplitude modulation mode

The most widely employed AFM mode for topography imaging is the AM-AFM, where the cantilever is used as a resonator. The basic principle of this AFM imaging mode consist in mechanically exciting the tip at a frequency close to its resonance value with a free oscillation amplitude ranging of few nm.[19] As the tip approaches the surface, the amplitude of the cantilever will decrease due to tip-surface interaction forces dampening the cantilever energy. This allows for the use of the cantilever amplitude as the feedback signal. In addition topography images generated during a scan, there is also information obtained from the phase image, which is the phase shift between the driving oscillation and the resultant cantilever oscillation while interacting with the surface. Extra information about the elastic properties of a sample can be obtained from this image, since the phase shift is sensitive to energy loss/dissipation of the tip to the sample.

Depending on the tip – sample interaction, as can be seen in Figure 2.5, this mode can be classified in a) non – contact: attractive regime, and b) intermittent contact or tapping: repulsive regime. Moreover, this mode has triggered other modes that are used to sense long range interaction.

2.3 Contact Resonance Frequency

Mechanical vibrations of a cantilever in contact with a surface have been used for a long time to study surface mechanical properties. The first names given to this technique were Atomic Force Acoustic Microscopy (AFAM)[20] and Ultrasonic Force Microscopy (UFM)[21] –named after the use of a certain range of mechanical excitation frequencies, which usually considers the application of frequencies below 100 kHz for AFAM and frequencies in the kHz-MHz range for UFM- and are based on the application of a mechanical excitation to the sample holder to induce vibrations to the sample, and detect them by a cantilever used as a force sensor in contact with a surface.

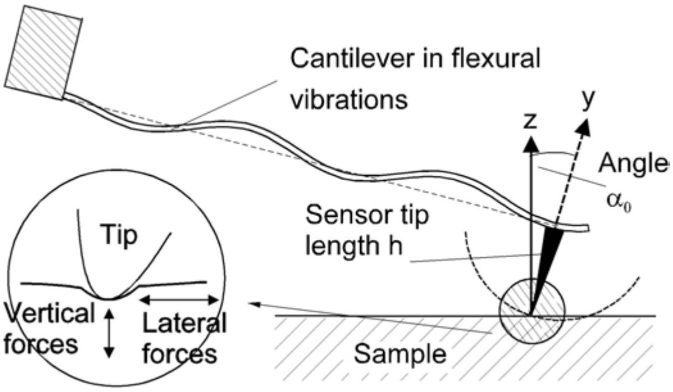

Figure 2.6: *Principle of the contact resonance force microscopy. The AFM cantilever can be described as a flexural beam a clamped end. Taken from [22].*

Contact Resonance Frequency Microscopy (CRF) is an advanced mode of contact AFM, based on the principle that when an AFM cantilever is placed into contact with the sample, its resonant vibration modes depend on both, the geometrical and materials properties of the cantilever (which are assumed to be constant for the whole measurement) and the tip-sample contact mechanical characteristics. In this sense, the tip-sample mechanical coupling strongly dominates the cantilever resonant properties, more specifically the contact resonance frequency and amplitude, which thus become sensitive to changes on the sample stiffness.

In this technique, the tip is brought into contact with the sample, and the system (tip-sample) is oscillated by a mechanical excitation, in order to promote flexural vibrations in the cantilever, as can be observed in Figure 2.6.

This mechanical excitation can be applied either to the sample or to the tip, typically using an acoustic stage or a piezo shaker as in our case. During the scanning process, the force between the tip and the sample is kept constant, and the frequency response of the tip-sample coupled system is measured. Owing to the fact that differences in the stiffness of the scanned area change the mechanical contact between the tip and the sample, and thus the contact resonance frequency; shifts in the measured frequency are proportional with the stiffness of the sample. However, in order to acquire quantitative measurements regarding material properties, tip-surface interactions need to be defined using appropriate models.

In this regard, Rabe and co-workers [23] developed a linear beam model that described the cantilever movement while it is in contact with the sample: the tip – surface interactions are modelled with dashpots and springs (see Figure 2.7) and the cantilever dynamics with two fixed ends is described by:

$$EI\frac{\partial^4 y}{\partial x^4} + \eta_{air}\rho A\frac{\partial y}{\partial t} + \rho A\frac{\partial^2 y}{\partial t^2} = 0 \tag{2.9}$$

For the simplest case in which we neglect the lateral damping and stiffnes, and assuming the Hertzian model for the tip-sample mechanical coupling, [24] a primarily constitutive

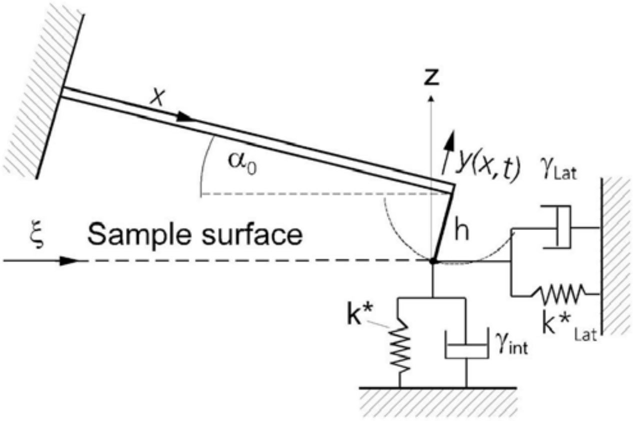

Figure 2.7: *Linear model of the cantilever while the tip is in contact with the substrate. Taken from [22].*

equation for contact stiffness (k*) is obtained:

$$-\frac{\partial F_H}{\partial z} = k* \sqrt[2]{6E*^2 RF_N} \tag{2.10}$$

Where the effective Young Modulus of the contact is obtained as:

$$\frac{1}{E*} = \frac{1-\nu_s^2}{E_s} + \frac{1-\nu_T^2}{E_T} \tag{2.11}$$

The contact resonance frequency obtained from the solution of this equation is:

$$\omega = \sqrt{\frac{k*+k_C}{m*}} = \omega_0\sqrt{1+\frac{k*}{k_C}} \tag{2.12}$$

Where ω_0 is the contact resonance frequency of an infinite stiff cantilever with the same geometry. From this equation, it is straightforward to observe that the contact resonance frequency is proportional to the sample stiffness and so that simply tracking variations in the contact resonance in a composite structure, various materials can be distinguished with respect to different stiffness values.[25] For increasing sample stiffness, one can observe a shift to higher contact resonance frequencies and vice versa. Furthermore, contact stiffness measurements can be transformed into elastic material properties such as elastic modulus, indentation modulus and viscosity by applying contact mechanics theories. [26]

All these improvements in the quantification of the tip – sample interactions over the years, have made of CRF an effective and well-established tool, which is implemented to acquire topographical maps of the elastic properties of materials at the nanoscale,[22, 27, 28] such as, polymers,[29-30] ferroelectric ceramics[31-34] and thin films.[35]

2.4 Piezoeresponse Force Microscopy

Piezoresponse Force Microscopy (PFM) is an advanced mode of contact AFM, based on the inverse piezoelectric effect (described in § 1.2.1). This mode, developed originally for imaging domain structures in ferroelectric materials,[36] has become a powerful tool to examine the local electromechanical phenomena of many materials, such as inorganic ferroelectric,[37-42] piezoelectric and ferroelectric,[43-46] energy storage devices,[47-49] perovskite for solar cell devices,[50] biological systems,[51-52] complex tissues,[53] to mention a few.

2.4.1 Operating principle

In standard measurements a periodic ac voltage is applied to a conductive tip, which is brought into contact with the surface of the sample and serving as an electrode

$$V_{tip} = V_{ac}\cos(\omega t). \tag{2.13}$$

This voltage generated oscillating electric field below the tip induces localized deformations of the sample surface via the inverse piezoelectric effect. The resulting cantilever deflection vibration is separately analysed by a lock-in amplifier, and the obtained amplitude and phase of these electromechanical vibrations provide information on the piezoelectric magnitude and orientation. The local piezoelectric response of the surface is detected as the first harmonic component, $A_{1\omega}$, of the tip deflection

$$A = A_{1\omega}\cos(\omega t + \varphi) \tag{2.14}$$

where φ is the phase difference between the applied voltage and the piezoresponse, which gives information related to the sign of the local piezoelectric coefficient.

Depending on the piezoelectric tensor the sample deformation under an applied vertical electric field can be in form of elongation, contraction or shear. Thus by combining the detection of lateral and vertical cantilever deflections (giving rise to two operating modes in PFM illustrated in Figure 2.8), it is possible to distinguish out-of-plane piezo-response and in-plane piezoresponse. The working principle of these two PFM operating mode are explained in § 2.3.2. Others forces, such as electrostatic forces between tip and sample surface charge, and electrostatic forces between the body of the cantilever and the sample surface charge, can also lead to undersired electromechanical response of the cantilever. [55-56] To minimize this non-desirable coupling, since in this case the oscillation induced by the electrostatic forces will depend on the cantilever stiffness, it is recommended to use stiff cantilevers.

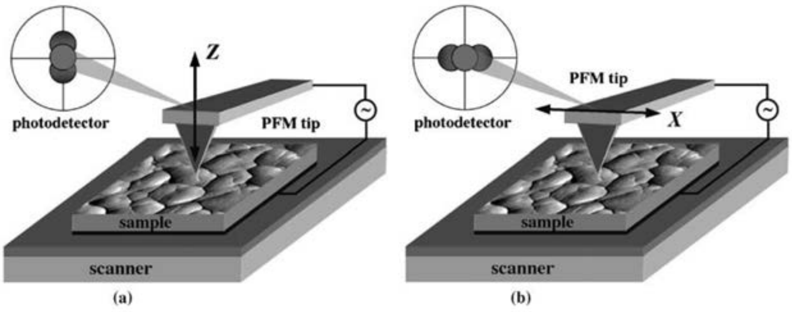

Figure 2.8: *Schematics of the vertical (a) and lateral (b) PFM signal detection. Taken from[54]*

The detection of absolute values of surface displacements under electrical fields of few volts is challenging, since for many samples these remain in the range of few pm. Thus, a natural way to enhance the tiny natural inverse piezoelectric effect is the use of the contact resonance frequency of the cantilever which will magnify the signal with an amplification factor proportional to the quality factor of the resonance:

$$A = d_{33}V_{ac}Q. \tag{2.15}$$

However, this remains hitherto a considerable challenge, because although working in resonance improves the piezoelectric response signal, other factors related to changes in the tip – sample mechanical coupling such as topography can make a shift in the resonance and induce crosstalk between the topography and the measured piezoresonse phase and amplitude. In order to overcome these problems two techniques can be applied: Dual AC Resonance Tracking (DART)[57] PFM and Band Excitation (BE)[58] PFM. The method used in the experimental part of this thesis for PFM measurements is DART – PFM, discussed in more detail in § 2.3.3.

2.4.2 Vertical and lateral PFM

Vertical PFM (VPFM) is the mode that allows to map the out-of-plane polarization by detecting the vertical flexural vibrations of the cantilever. [36] The surface displacement (amplitude) in this case is proportional to the longitudinal piezoelectric coefficient, and is given by

$$\Delta z = d_{33} V_{ac} \tag{2.16}$$

The application of a positive tip bias over a ferroelectric sample with downward polarization (c^-) results in the expansion of the sample (see Figure 2.9(a)) and the surface oscillates in phase with the tip voltage, thus $\varphi = 0°$. Whereas in a ferroelectric sample with upward

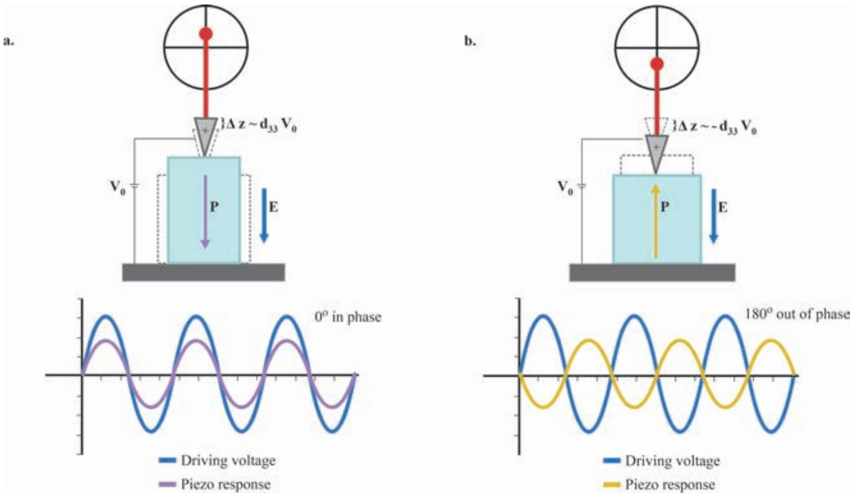

Figure 2.9: *Schematic illustration of vertical PFM.*

polarization (c^+) the application of a positive tip voltage results in the contraction of the sample (see Figure 2.9(b)) and the sample oscillates out phase, therefore $\varphi = 180°$.

On the other hand, lateral PFM (LPFM) is the mode that maps the in-plane polarization by detecting the twist or perpendicular torsion of the cantilever thanks to frictional forces.[42] For piezoelectric/ferroelectric samples with in plane polarization, and corresponding shear coefficients of the piezoelectric tensor, the application of an out of plane voltage generates a shear movement translated via the friction forces to the torsional movement of the cantilever, that can be detected as a lateral signal in the photodiode (See Figure 2.10). The quantification in LPFM is challenging due to the tip-surface tribology, inhomogeneous field distribution and mechanical clamping effects, and more specifically due to the difficulty in the calibration of lateral cantilever stiffness. Nevertheless, as long as the in-plane polarization vector is perpendicular to the physical axis of the cantilever the amplitude of the in – plane oscillation, i.e. the shear piezoelectric coefficient, is proportional to:

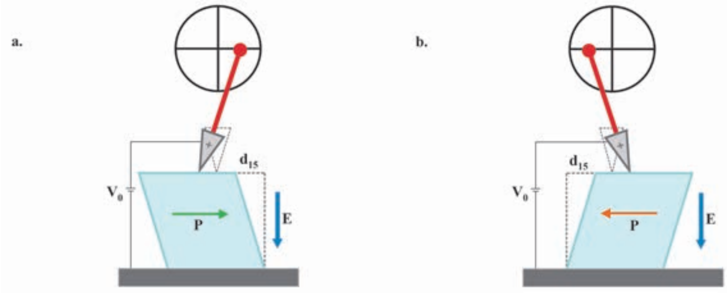

Figure 2.10: *Schematic illustration of lateral PFM.*

$$\Delta x = d_{15} V_{ac} \tag{2.17}$$

Finally, in-plane piezoelectric response oriented parallel to the cantilever axis can induce an out of plane deflection detected as a vertical PFM signal due to cantilever buckling.

2.4.3 DART PFM

DART is a methodology used for the detection of a resonance frequency that applies when Phase-Lock loop techniques are not recommendable, mostly because of signal's phase instability. In this method the tip applied ac voltage is modulated simultaneously at two frequencies, (f_1, f_2) one above and the other below the resonance peak (f_0) with a certain bandwidth, as can be observed in Figure 2.11. [59] In DART PFM the signal of the amplitude and phase at both frequencies is recorded by two lock-in amplifiers, and the difference between the two amplitude responses, $\Delta A = A_1$ - A_2, is taken as an error signal for the feedback loop. This difference is minimized in order to maintain the cantilever oscillations at both frequencies at the same level by adjusting the frequencies, thus allowing for tracking of the resonance frequency. By measuring the PFM signal at the contact resonance frequency, one optimizes the piezoelectric response signal by minimizing

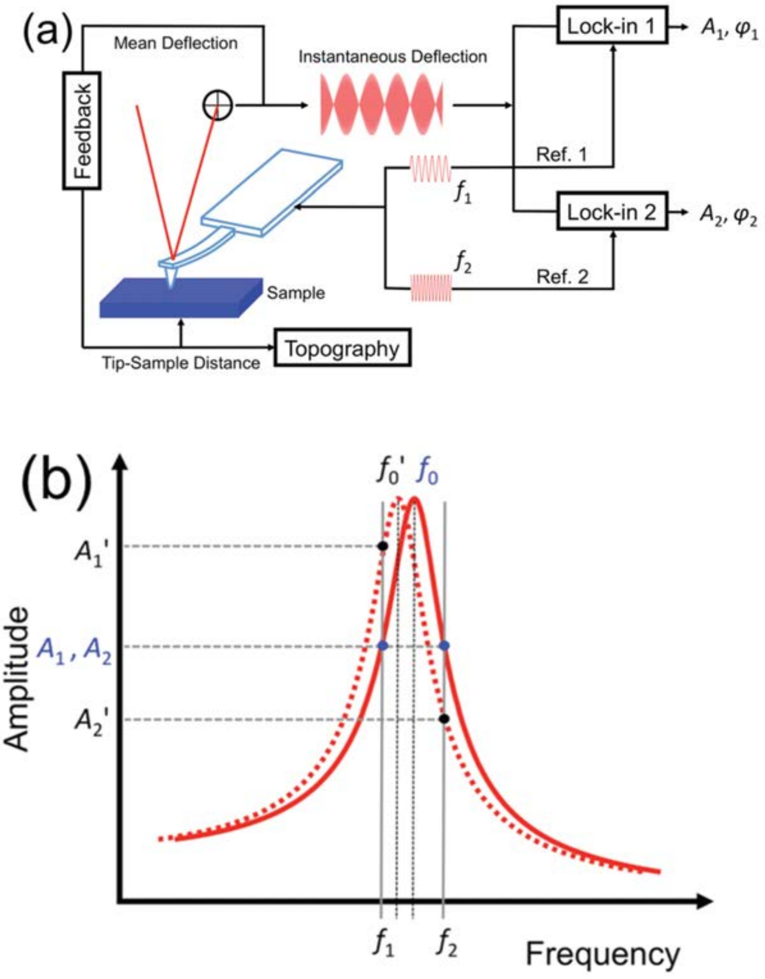
(a)
Mean Deflection
Instantaneous Deflection
Feedback
Lock-in 1
A_1, φ_1
Ref. 1
f_1
Lock-in 2
A_2, φ_2
f_2
Ref. 2
Sample
Topography
Tip-Sample Distance
(b)
f_0' f_0
A_1'
A_1, A_2
A_2'
Amplitude
f_1
f_2
Frequency

Figure 2.11: *Principle of dual AC resonance tracking piezoresponse force microscopy. (a) Scheme and (b) contact resonant frequency tracking principle. Taken from [59]*

the topography crosstalk and other mechanical effects leading to shifts of the contact resonance frequency.

References

1. Mohs, F. *Grundriss der Mineralogie.* 1822, Dresden.
2. Hertz, H. *J. Reine Angew. Math.* 156 – 171 (1881).
3. Sneddon, N. *Inter. J. Eng. Sci.* **3(1)**: 47-57 (1965).
4. Oliver, W.C& Bolshakov. A. *J Mater Res.* **17**, 2660 – 2671 (2002).
5. Oliver, W.C.& Pharr, G.M. *J. Mater. Res.* **19**, 3-20 (2004).
6. Fischer-Cripps, A.C. *Sur. Coat. Technol.* **200**, 4153 – 4165 (2006).
7. Fischer-Cripps, A.C. *J. Mater. Res.* **16(7)**, 2149-2157 (2001).
8. Fischer-Cripps, A.C. *Mater. Sci. Eng.* **A 385**, 74-82 (2004).
9. Binnig, G., Rohrer, H., Gerber, C. & Weibel, E. *Phys. Rev. Lett.* **49**, 57 (1982).
10. Binnig, G., Quate, C. F. & Gerber, C. *Phys. Rev. Lett.* **56**, 930 (1986).
11. Giessibl F.J. *Science* **267**, 5194 (1995)
12. García R. & Pérez R. *Surf. Sci. Rep.* **47**,197 – 301 (2002).
13. Giessibl F.J. *Rev. Mod. Phys.* **75**, 949 (2003).
14. Hofer W.A., Foster A.S., & Shluger A.L. *Rev. Mod. Phys.* **75**, 1287 (2003).
15. Martin, Y., Williams, C.C.& Wickramasinghe, H.K. *J. Appl. Phys.* **61**, 10 (1987).
16. Zhonng, Q. & Inniss, D. *Surf. Sci. Lett.* **290**, 688 – 692 (1993).
17. Albrecht, T.R., Gutter, P., Horne, D. & Rugar, D. *J. Appl. Phys.* **62**, 2 (1991).
18. San Paulo, A. & Garcia, R. *Phys Rev B.* **64**, 193411 (2001).
19. Rabe, U. & Arnold, W. *Appl. Phys. Lett.* **64**, 1493 (1994).

20. Yamanaka, K., Ogiso, H. Kolosov, O. *Appl. Phys. Lett.* **64**, 178 (1994).

21. Rabe, U., Turner, J. & Arnold, W. *Appl. Phys. A* **66**, S277-S282 (1998).

22. Rabe, U., Janser, K. & Arnold, W. *Rev. Sci. Instrum.* **6**7, 3281-3293 (1996).

23. Johnson KL. *Contact Mechanics.* Cambridge University Press: Cambridge (1995).

24. Rabe, U., Amelio, S., Kopycinska, M., Hirsekorn, S., Kempf, M., Goken, M. & Arnold, W. *Surf. Interface Anal.* **33**, 65-70 (2002).

25. Kopycinska-Muller, M., Geiss, R. H. & Hurley, D. C. *Ultramicroscopy* **106**, 466-474 (2006).

26. Yamanaka, K. & Nakano, S. *Appl. Phys. A* **66**, S313-S317 (1998).

27. Rabe, U., Kopycinska, M., Hirsekorn, S. & Arnold, W. *Ultrasonics* **40**, 49-54 (2002).

28. Hurley, D. C., Kopycinska-Müller, M., Kos, A. B. & Geiss, R. H. *Meas. Sci. Technol.* **16**, 2167-2172 (2005).

29. Killgore, J. P., Yablon, D. G., Tsou, A. H., Gannepalli, A., Yuya, P. A.,. Turner, J. A, Proksch, R. & Hurley, D. C. *Langmuir* **27**, 13983-13987 (2011).

30. Abplanalp, M., Eng, L.M. & Günter, P. *Appl Phys A* **66**, S231-S234 (1998).

31. Eng, L.M., Abplanalp, M. & Günter, P. *Appl Phys A* **66**, S679-S683 (1998).

32. Rabe, U., Amelio, S., Kester, E., Scherer, V., Hirsekorn, S. & Arnold, W. *Ultrasonics* **38**, 430-437 (2000).

33. Rabe, U., Kopycinska, M., Hirsekorn, S., Muñoz-Saldaña, J., Schneider, G. A. & Arnold, W.J. *Phys. D: Appl. Phys.* **35**, 2621–2635 (2002).

34. Passeri, D., Bettucci, A. & Rossi, M. *Anal Bioanal Chem* **396**, 2769-2783 (2010).

35. Günther, P., Glatz-Reichenbach, J. & Dransfeld, K. *J. Appl. Phys* **69**, 7895-7897 (1991).

36. Gruverman, A., Auciello, O. & Tokomuto, H. J. *Vac. Sci. Technol.* **14**, 602 (1996).

37. Gruverman, A., Auciello, O. & Tokomuto, H. *Appl. Phys. Lett.* **69**, 3191 (1996).

38. Zavala, G., Fendler, J. H. & Trolier-McKinstry, S. *J. Appl. Phys.* **81**, 7480 (1997).

39. T. Tybell, C. Ahn and J. -M. Triscone. *Appl. Phys. Lett.* **72**, 1454 (1998).

40. O. Auciello, A. Gruverman, H. Tokumoto, S. A. Prakash, S. Aggarwal and R. Ramesh. *MRS Bull.* **23**, 33 – 42 (1998).

41. Abplanalp, M., Eng, L. & Günter, P. *Appl. Phys. A-Mater.* **66**, S231 - S234 (1998).

42. V. Shvartsman, A. Kholkin, M. Tyunina, and J. Levoska. *Appl. Phys. Lett.* **86**, 222907 (2005).

43. V. Shvartsman and A. Kholkin. *J. Appl. Phys.* **101**, 064108 (2007).

44. S. V. Kalinin, B. J. Rodriguez, J. D. Budai, S. Jesse, A. N. Morozovska, A. A. Bokov, and Z. G. Ye.

45. A. Kholkin, A. Morozovska, D. Kiselev, I. Bdikin, B. Rodriguez, P. Wu, A. Bokov, Z. G. Ye, B. Dkhil, and L. Q. Chen. *Adv. Funct. Mater.* **21**, 1977 (2011).

46. K. M. Abraham and Z. Jiang. *J. Electrochem. Soc.* **143**, 1 (1996).

47. N. Balke, S. Jesse, A. N. Morozovska, E. Eliseev, D. W. Chung, Y. Kim, L. Adamczyk, R. E. Garcia, N. Dudney and S. V. Kalinin. *Nat. Nanotech.* **5**, 749 (2010).

48. N. Balke, S. Jesse, Y. Kim, L. Adamczyk, A. Tselev, I. N. Ivanov, N. J. Dudney and S. V. Kalinin. *Nano Lett.* **10**, 3420 (2010).

49. Y. Kutes, L. Ye, Y. Zhou, S. Pang, B. D. Huey and N. P. Padture. *J. Phys. Chem. Lett.* **5**, 3335 (2014).

50. S. V. Kalinin, B. J. Rodriguez, S. Jesse, T. Thundat, and A. Gruverman. *Appl. Phys. Lett.* **87**, 053901 (2005).

51. S. V. Kalinin, E. Eliseev, and A. Morozovska. *Appl. Phys. Lett.* **88**, 232904 (2006).

52. Y. M. Liu, Y. J. Wang, M. J. Chow, N. Q. Chen, F. Ma, Y. Zhang, and J. Li. *Phys. Rev. Lett.* **110**, 168101 (2013).

53. Gruverman, A.& Kalinin, S.V. *J. Mater. Sci.* **41**, 107 – 116 (2006).

54. C. Harnagea, M. Alexe, D. Hesse, and A. Pignolet. *Appl. Phys. Lett.* **83**, 338 (2003).

55. B. D. Huey, C. Ramanujan, M. Bobji, J. Blendell, G. White, R. Szoszkiewicz, and A. Kulik. *J. Electroceram.* **13**, 287 (2004).

56. B. J. Rodriguez, C. Callahan, S. V. Kalinin, and R. Proksch. *Nanotechnology* **18**, 475504 (2007).

57. S. Jesse, S. Kalinin, R. Proksch, A. P. Baddorf, and B. Rodriguez. **Nanotechnology** **18**, 435503 (2007).

58. Liu, Na., Dittmer, R., Stark, R.W. & Dietz, C. *Nanoscale* **7**, 11787 (2015).

Part II

Results and discussion

CHAPTER 3

Switchable mechanical properties of ferroelectrics

The mechanical properties of materials, such as hardness, stiffness, and fracture toughness, are in principle insensitive to space inversion, i.e. they should be the same irrespective of whether they are measured in one direction or in the opposite direction of the material. As explained in the introduction, this principle derives from the fact that the magnitudes used to describe the mechanical properties, i.e. stress, strain, and elastic constants, are all even parity tensors. This mathematical argument is also valid for cristallographically asymmetric materials such as ferroelectrics, and physically this means that the mechanical response of a ferroelectric material should not depend on the sense of the polarization direction. However, symmetry restrictions can change drastically when the applied deformations are inhomogeneous.[1, 2, 3, 4]

This chapter present the research on the effects of flexoelectricity on the energy cost and the mechanical properties of uniaxial ferroelectrics. Firstly, it will be shown, by intuitive and rigorous conceptual arguments, that in uniaxial ferroelectrics the presence of strain gradients must induce asymmetry in their mechanical response. Secondly, it will be demonstrated experimentally using nanoindentation that both plastic and elastic mechanical responses of ferroelectric materials become asymmetric under strain gradients. Finally, it will be shown that, from the experimental results, it is possible to estimate the flexocoupling coefficient of uniaxial ferroelectrics.

3.1 Energy cost of deforming piezoelectric and ferroelectric materials

Deforming a material that is electromechanically active, and therefore generates a polarization P in response to the deformation, has an associated energy cost, which will be different depending on whether the deformation is homogeneous or inhomogeneous. In general this energy cost is given by

$$U = \frac{1}{2}k\varepsilon^2 + \frac{1}{2}\frac{P^2}{\chi}, \tag{3.1}$$

where k is (one of) the elastic constant(s), ε is (a component of) the strain field, χ is the electric susceptibility, and P is the polarization induced by the deformation. This expression shows explicitly that there are two contributions: an elastic one (first term), associated with the deformation itself (Hooke's law), and an electrostatic one (second term), associated with the deformation-induced polarization.

3.1.1 Energy cost under homogeneous deformation

In a piezoelectric, when the deformation is homogeneous, the energy cost will be the same even if the space inversion is changed. The reason for this equality lies in the fact that in the electrostatic energy the polarization is squared, and thus insensitive to the sign of the piezoelectric coefficient, so turning a piezoelectric crystal upside down will not make any difference in the electrostatic energy cost and therefore in the mechanical response of the crystal.

In a ferroelectric, which is a switchable piezoelectric, the reasoning is the same than before: under homogeneous deformation, the electrostatic and mechanical energies of the material are symmetrical with respect to space inversion and thus the total deformation energy costs of the two opposite polar states are equal.

3.1.2 Energy cost under inhomogeneous deformation

When the deformation is inhomogeneous, the situation changes. In a piezoelectric, there will be two sources of polarization: the strain itself, via piezoelectricity, and the strain gradient, via flexoelectricity, and these two polarizations can be parallel or antiparallel depending on the sign of the piezoelectric coefficient of material. Thus, the same inhomogeneous deformation generates an enhanced polarization when piezoelectricity and flexoelectricity are parallel ($P = P_{piezo} + P_{flexo}$) and a reduced polarization if they are antiparallel ($P = -P_{piezo} + P_{flexo}$). The cost of the electrostatic energy, described in equation (3.1), still depends on the square of the total polarization (P^2), but now the *magnitude* of $\mathbf{P}$ itself is different depending on the sign of P_{piezo}. This difference in the magnitude of the induce polarization results in an electrostatic energy cost unequal and thus asymmetric with respect to space inversion. The asymmetry of the electrostatic energy cost implies that the elastic response of a piezoelectric material under the presence of inhomogeneous deformation becomes also asymmetric.

Additionally, in the case of a ferroelectric, the electrostatic energy cost by deforming it in an inhomogeneous way has an extra component due to the interaction of the flexoelectric field with the ferroelectric dipole. The total electrostatic energy cost in this case is given by:

$$U_{elec} = \frac{1}{2}\frac{P^2}{\chi} - E_{flex}P_0, \tag{3.2}$$

where E_{flex} is the flexoelectric field induced by the inhomogeneous deformation, and P_0 is the ferroelectric polarization. This expression entails that, besides the asymmetry induced by the piezoelectricity ± flexoelectricity explained above, there is an additional energy cost due to the interaction between flexoelectric field and the ferroelectric polarization which is also asymmetric with respect to the polarity of the ferroelectric material.

Moreover, this interaction between the flexoelectric field and the ferroelectric polarization can provide a source for energy dissipation if the flexoelectric field generated is sufficient strong to switch the polarization.[5] Thus, strain gradients in principle can also affect mechanical energy dissipation and therefore plastic deformation.

3.2 Free energy of ferroelectric materials

The role of flexoelectricity on the electrical, mechanical, and electromechanical response of ferroelectrics can be also be rigorously exposed by incorporating flexoelectricity in the free energy of ferroelectrics: [6, 7]

$$\begin{aligned} G = \int \Bigg[&\frac{1}{2}\alpha_{ij}P_iP_j + \frac{1}{4}\beta_{ijkl}P_iP_jP_kP_l + \frac{1}{2}\gamma_{ijklmn}P_iP_jP_kP_lP_mP_n \\ &+ \frac{1}{2}C_{ijkl}\varepsilon_{ij}\varepsilon_{kl} - \frac{1}{2}q_{ijkl}\varepsilon_{ij}P_kP_l \\ &+ \frac{1}{2}g_{ijkl}P_{i,j}P_{k,l} - f_{ijkl}P_k\frac{\partial \varepsilon_{ij}}{\partial x_l}\Bigg] dV \end{aligned} \tag{3.3}$$

where the first three terms represent the Landau free energy density with the phenomenological Landau-Devonshire coefficients,[8] P_i is the total polarization component, and ε_{ij} is the strain component. The fourth term denotes the elastic energy density of the system and c_{ijkl} is the elastic tensor. The fifth term indicates the coupling energy density between the polarization and strain, where q_{ijkl} is the electrostrictive tensor. The sixth term is the polarization gradient energy density and g_{ijkl} is the correlation energy tensor.

The last term in equation (3.3) is the flexoelectric coupling energy density, and f_{ijkl} is the flexocoupling tensor describing both direct and converse flexoelectric effects.[3, 9] This term, the flexoelectric energy, is the only one that is an odd function of polarization, and is therefore responsible for introducing a difference in the free energy of two opposite polar states which must lead to an asymmetric material response.

From equation (3.3) it is possible to calculate the free energy difference between the positively (P^+) and the negatively (P^-) polarized states in the presence of a strain gradient. The free energy difference can be obtained from the following equation:

$$\Delta G = G^+ - G^- = \int \left[f_{ijkl}P_k^-\frac{\partial \varepsilon_{ij}}{\partial x_l} - f_{ijkl}P_k^+\frac{\partial \varepsilon_{ij}}{\partial x_l} \right] dV \tag{3.4}$$

This equation shows explicitly that the incorporation of strain gradients breaks the equivalence between polar states, since otherwise the energy difference between the upward state and the downward state would be zero. Furthermore, this difference in free energy indicates that mechanical responses depend on the direction of the ferroelectric polarization. In this respect, Abdollahi et al have made the prediction that, due to the fact that flexoelectricity is a size-dependent property,[10] $BaTiO_3$ thin films of the right thickness and with a given polarity should be twice as easy to crack than in the opposite direction.[6] Previous nanoindentation experiments on ferroelectrics have shown a strong size-dependent stiffening[11-12] (although symmetry effects were not explored), while in relaxors an electric-field-dependent elastic modulus[7] that were attributed to flexoelectricity caused by the inhomogeneous strain field produced by a nanoindenter. Motivated by these results and the reasoning of the differences in the energy cost described in the previous section, the mechanical properties of uniaxial ferroelectrics were investigated using the nanoindentation technique, which enables us to mobilize the flexoelectric effect around a sharp indenter tip, as shown in figure 3.1, while simultaneously probing the mechanical response of the material. The results of this investigation are described herein.

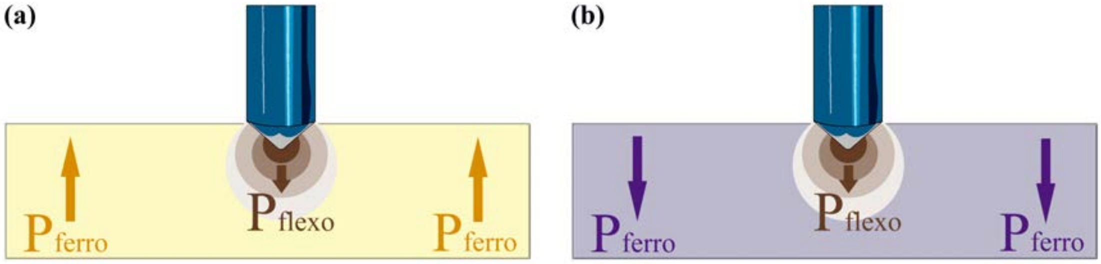

Figure 3.1: *Scheme of the flexoelectric polarization (arrows) induced by the inhomogeneous deformation generated with an indenter tip on a uniaxial ferroelectric with (a) polarization pointing down, and (b) polarization pointing up*

3.3 Experiment

The material chosen for this study were single crystals of Lithium Niobate ($LiNbO_3$) z-cut, i.e. with polarization perpendicular to the surface. This material was chosen because its ferroelectric phase transition is non-ferroelastic, meaning that only 180°domain switching is possible. This feature prevents any stress-induced ferroelastic reorientation of the polarization,[13] thus simplifying the analysis and guaranteeing that any evidence of domain switching under the indentation load must be due to flexoelectric effects.

It is well-known that, depending on Li^+ concentration, $LiNbO_3$ can be stoichiometric or congruent.[14, 15, 16] Here, both types of samples: stoichiometric and congruent, have been studied. The stoichiometric sample was single-domain (SLN) and has a large coercive field. In this case, inversion of polarization was achieved by simply cutting the crystal in two equal pieces and turning one half upside-down in order to study two areas with opposite polarization.

The congruent sample was a periodically poled $LiNbO_3$ single crystal (PPLN), which facilitates access to both polarities on the same side of the crystal. The size of each domain was $\sim 5\mu m$ as can be observed in figure 3.2. The three crystals were chemically cleaned by sonicating them for 15 min in acetone, isopropanol and MilliQ water sequentially. Finally,

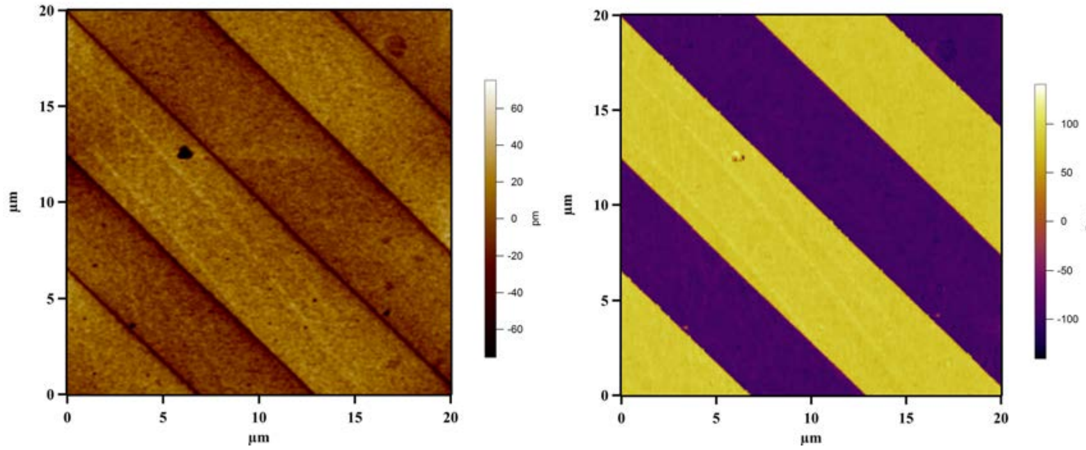

Figure 3.2: *PFM amplitude (left) and phase (right) image showing the periodic domain structure of the PPLN crystal where yellow correspond to upward polarization and purple correspond to downward polarization*

they were glued onto a metallic disc with silver paste. Nanoindentation experiments were carried out in the load-control mode, using a UMIS instrument from Fischer-Cripps Laboratories equipped with a Berkovich pyramidal-shaped diamond tip (Details of the technique are given in section 2.1). The thermal drift was always kept below ± 0.05 nms^{-1}. Indentations were first performed in the monodomain SLN crystal. In order to get statistically useful results, 50 indentations (25 for each polarity) were performed and analyzed for each mechanical load. Four different maximum loads (7 mN, 10 mN, 15 mN and 20 mN) were applied, i.e a total of 200 indentations. Indentations were arranged

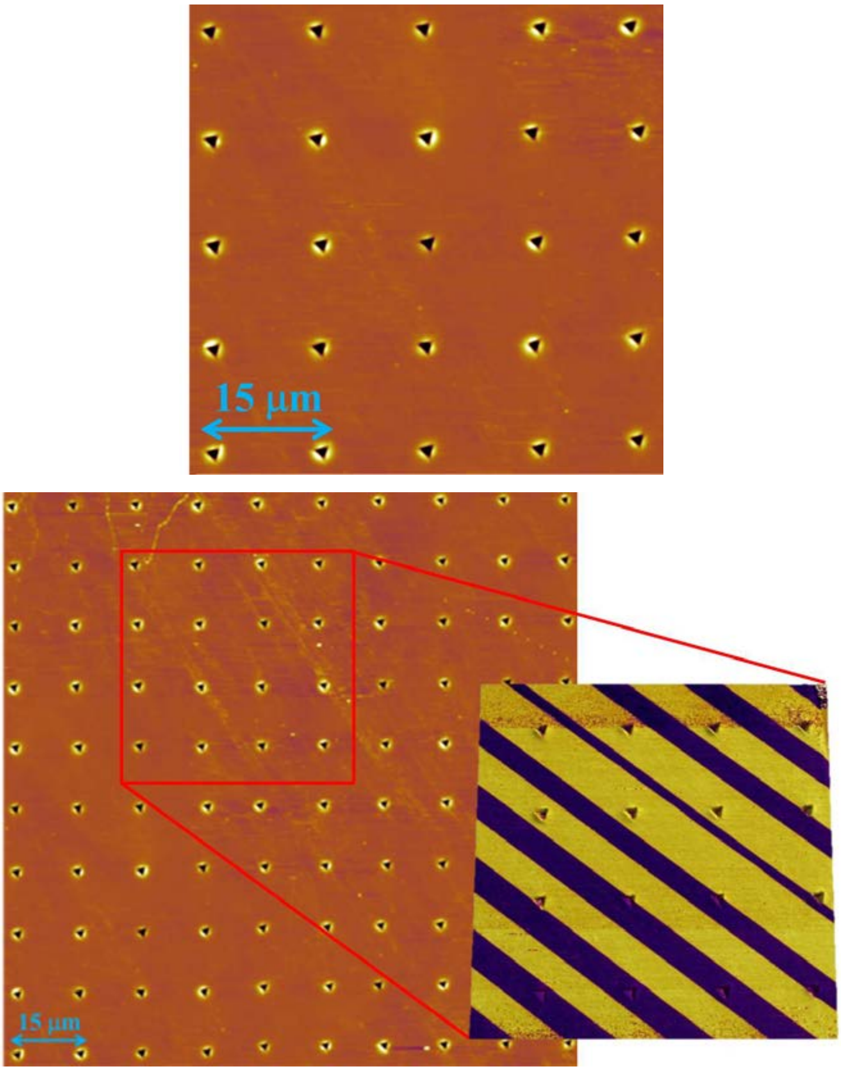

Figure 3.3: *(up) AFM topography image of the surface of an SLN crystal after performing 25 nanoindentations with the same indentation force. (downt) PFM topography and phase image of the surface of a PPLN crystal after performing 100 nanoindentations with the same indentation force.*

in arrays of 5x5, and spaced 15 μ m apart ensuring a sufficient independence of the indentations in all cases. (See figure 3.3 up). In the case of PPLN, five different maximum loads (5 mN, 7 mN, 10 mN, 15 mN and 20 mN) were applied. In this sample, some indentations can fell on domain walls, therefore in order to ensure that enough indentations fell integrally in the domains, 100 indentations per load, i.e. a total of 500 indentations, were performed and arranged in arrays of 10x10 and spaced 15 μ m as in SLN.

To correlate the direction of the polarization with each indentation in PPLN, PFM maps were measured using an Asylum MFP-3D AFM, and OMCL – AC240TM – R3 cantilevers, with a k $\sim$ 2 N/m. PFM was mainly operated in DART mode in order to benefit from resonance signal enhancement (see figure 3.3 down), and the right phase contrast was determined from measurements performed at single frequency well below the resonance frequency.

3.4 Mechanical and flexoelectric properties of LiNbO3 under indentation

In theory (section 3.2, equation 3.4), the presence of flexoelectricity in ferroelectric materials leads to an asymmetry of free energy. For the purpose of quantification, asymmetry is here defined as

$$\%Asym \equiv 100\frac{\langle M^{+}\rangle - \langle M^{-}\rangle}{\langle M\rangle} \tag{3.5}$$

where $\langle M^{+}\rangle$ - $\langle M^{-}\rangle$ is the difference between the average mechanical indentation energies of the up-polarized and down-polarized states, respectively, and $\langle M\rangle$ is the mean for all polarities. Positive asymmetry indicates a larger value for the upward polarization, whereas negative asymmetry indicates that downward polarization is bigger.

3.4.1 Indentation measurements on stoichiometric LiNbO3

Figure 3.4 (a) shows, for the stoichiometric sample, the asymmetry of the different energies as obtained from indentation experiments as a function of the applied load. As can be observed, the total energy (elastic + plastic) is essentially symmetric, consistent with the fact that the energy provided by the indenter is independent of the sample polarity, as should be expected. This provides a useful "sanity check" to ensure that the asymmetries of other magnitudes are not artifacts introduced by the measurement apparatus. In contrast, an asymmetric behavior can be observed both for the plastic and for the elastic energy.

Plastic energy concerns the material properties related to energy dissipation. This dissipation can also be quantified by the plasticity index, a dimensionless parameter indicating the ratio of the plastic energy to the total energy i.e. Up / Ut. It has been demonstrated that fracture toughness, i.e. the measure of energy dissipation for propagating a crack, is an increasing function of the plasticity index. [17-18] The asymmetry of the plasticity index can be observed in figure 3.4(b) and is analogous to that of the plastic energy. The conclusion is therefore that the fracture toughness of ferroelectrics is indeed asymmetric. There is also an asymmetric behavior of the elastic energy (figure 3.4(a)), which implies that fracture toughness is not the only mechanical property sensitive to the polarization direction. Given that both plastic and elastic energies are asymmetric, all mechanical responses (dissipative such as fracture or conservative such as elasticity) are in principle polarity-dependent. Using the Oliver-Pharr metho,[19-20] described in section 2.1.3, we have extracted the following mechanical properties: (a) hardness, as a measure of the resistance to plastic deformation, and (b) contact stiffness, as a measure of the elastic response of the material. Both are found to be dependent on polarity: contact stiffness shows a negative asymmetry whereas hardness indicates a positive asymmetry, see figure 3.4(b).

These results demonstrate unambiguously that stoichiometric lithium niobate has two different types of mechanical response: downward polarized material is stiffer but more fragile, whereas upward-oriented material is more elastic but also tougher against indentation.

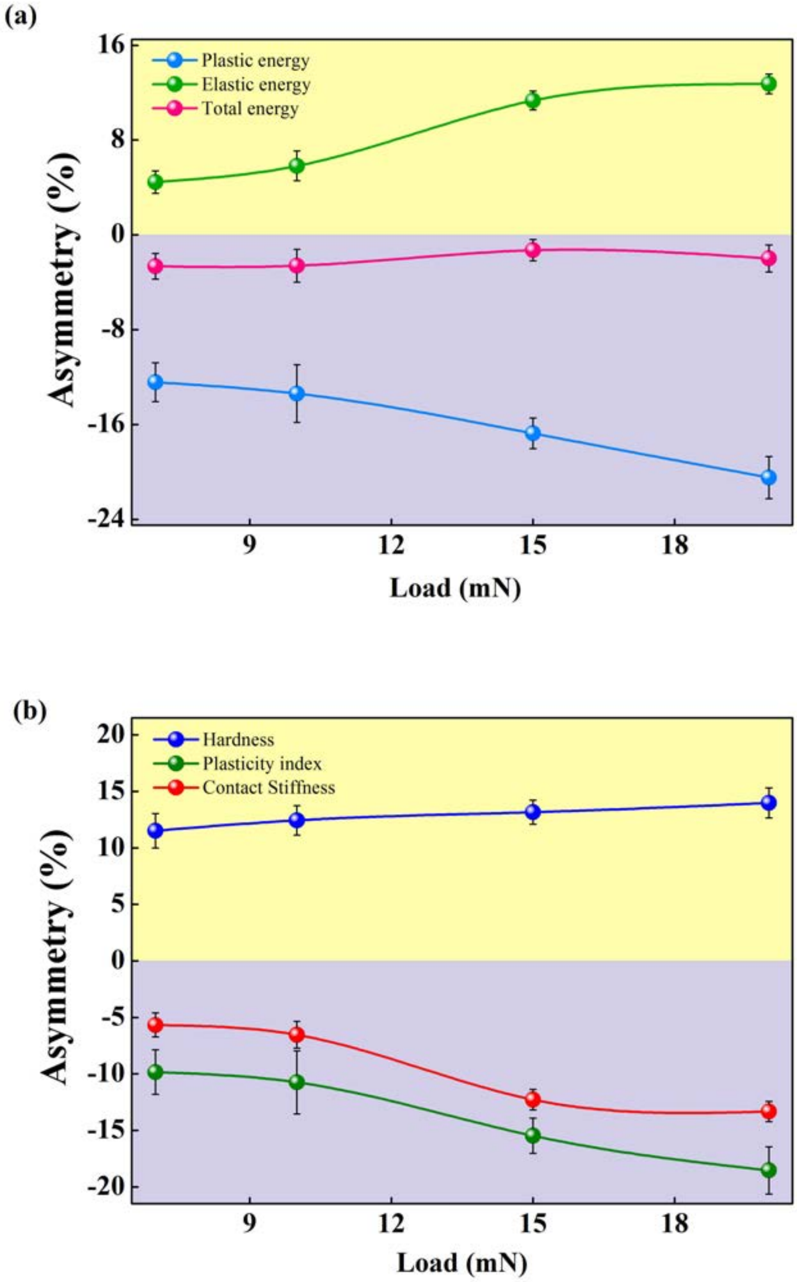

Figure 3.4: *Asymmetry behaviour of energies(a) and mechanical properties (b) as function of the maximum indentation load in SLN, showing that both plastic and elastic mechanical responses are asymetric.*

3.4.2 Indentation measurements on congruent LiNbO3

The PPLN samples were congruent instead of stoichiometric. The different stoichiometry results in a different absolute value of the asymmetry, as can be observed in Figure 3.5.

However the sign of the asymmetry at small loads (5 mN, 7 mN and 10 mN) in all the parameters were the same as that obtained in SLN. Since, for PPLN, all indentations are performed on the same surface and with the same orientation of the sample with respect to the indenter, the results rule out the possibility of a geometrical origin of the asymmetry and thus validate the conclusions. Given that in PPLN the ferroelectric polarization is switched in the conventional sense (as opposed to the crystal flipping done with SLN), the results also confirm that it is possible to use an external voltage to toggle between two different types of mechanical response: downward polarized material is stiffer but more fragile, while upward-oriented one is more elastic but tougher against indentation.

On the other hand, for higher loads (15 mN and 20 mN), it is interesting to observe that by increasing the indentation load, the asymmetry of the plastic energy changes sign, as opposed to SLN, i.e., there is more energy dissipation in domains with polarization pointing up that in domains with opposite polarization. At the same time, the asymmetry of the elastic energy decreases as the indentation load is increased. Furthermore, from Figure 3.5(b) it can be observed that the asymmetry of the plastic energy does not correspond to that of the stiffness, e.g. for the maximum indentation load of 20mN, the plastic energy shows the maximum asymmetry while the stiffness becomes almost symmetric. These evidences suggest that, in addition to plastic deformation, there are other mechanisms responsible for mechanical energy dissipation in ferroelectrics. We have observed that the additional energy dissipation comes from ferroelectric polarization switching. It is known that flexoelectricity can induce ferroelectric domain switching[5] in ferroelectric thin films. Here, thanks to the absence of 90°ferroelastic switching in $LiNbO_3$, we can in theory also expect 180°ferroelectric switching due to flexoelectricity.[3,5] The questions are, then: (i) does it really happen? i.e., does the indenter provide a sufficiently large flexoelectric field to be able to switch polarization in a macroscopic crystal, as opposed to the nanoscopically localized switching observed in thin films? (ii) Can switching explain the evolution of the mechanical asymmetry as a function of indentation load, and (iii) If the difference between mechanical behaviors of SLN and PPLN reflects differences in

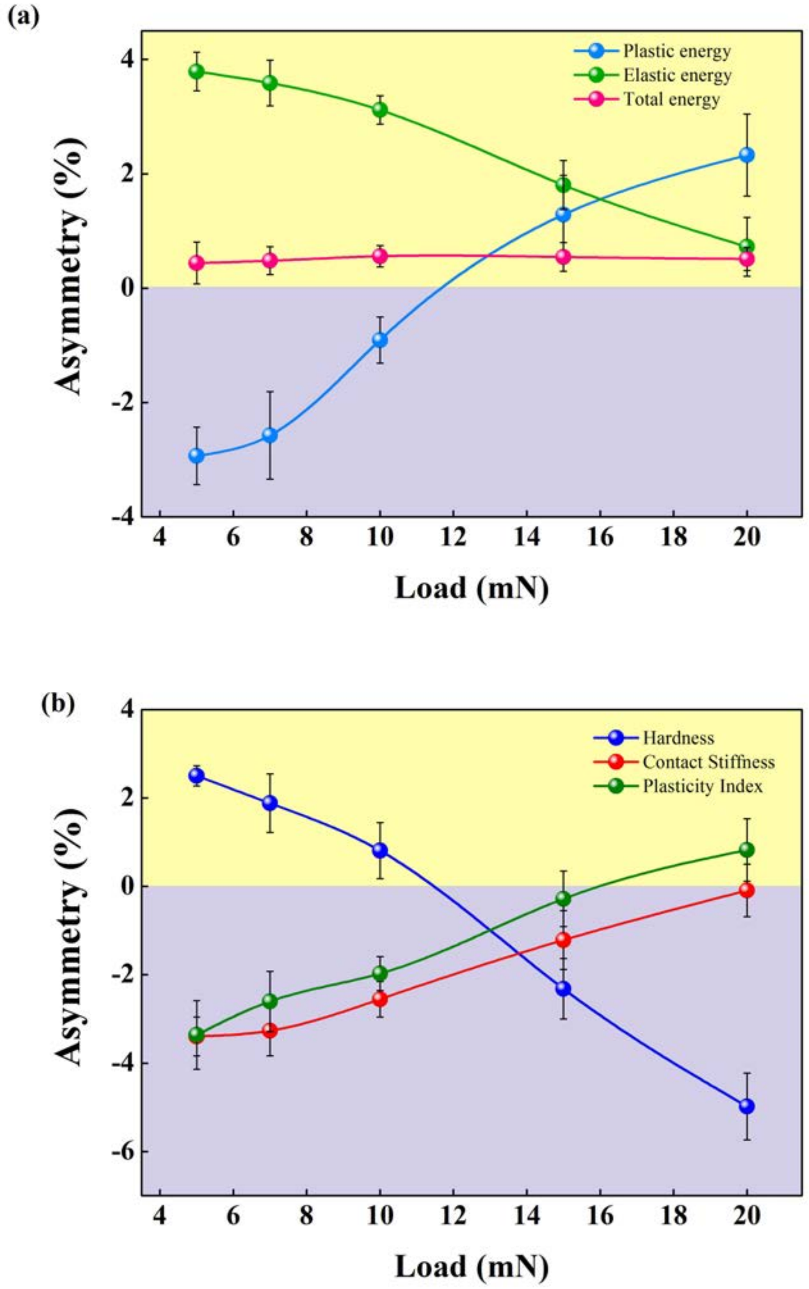

Figure 3.5: *Figure 3.5: Asymmetry behaviour of energies(a) and mechanical properties (b) as function of the maximum indentation load in PPLN, showing that both plastic and elastic mechanical responses are asymetric.*

flexoelectric switching behavior, what is the origin of this difference?

The basic idea of flexoelectric switching is as follows. Indentation induces a high localized compressive stress, so a large downward strain gradient is generated, resulting in an effective electric field due to the flexoelectric effect. This electric field is antiparallel to the polarization dipole for domains with polarization pointing up, providing the necessary input for flexoelectric switching in these domains. To examine this possibility, indentations in PPLN samples were investigated by PFM.

Figure 3.6 presents a 3D plot of topography with the superimposed PFM phase of a small area around the indentations. In the convention used in this thesis, the out of plane polarization pointing up is defined by a phase value of 180° that corresponds to the yellow contrast, whereas the opposite polarization is defined by a phase value of 0°, shown here as purple. It is clear that, upon increasing indentation load, flexoelectric switching begins to occur in the upward domains, thus increasing the energy dissipated in these domains as compared to the downward domains, where domain switching was absent for all loads. This can explain the evolution of the plastic energy asymmetry: as discussed earlier for figure 3.5(a), the change of sign of the asymmetry arises from the fact that, in addition to the energy dissipation due to fracture, upward polarization domains progressively introduce another source for energy dissipation, the flexoelectric polarization switching. The energy dissipated by switching is substracted from the total amount of energy available for inducing fracture, and hence the up-polarized domains become progressively tougher compared to the down-polarized domains.

Flexoelectric switching may have consequences for the asymmetry of other mechanical properties of ferroelectrics. For example, as shown in figure 3.5(b), the contact stiffness asymmetry also becomes weaker upon increasing the indentation load. Since the stiffness is determined upon unloading and therefore after flexoelectric switching has taken place, there is no longer any difference between the final polarities inside the indentations (see figure 3.6), and thus the initial difference between polarity-dependent properties such as stiffness also disappears. Although the flexoelectric switching explains the behavior of the asymmetries in the PPLN sample, a new question arises: Why there is no local switching in the SLN sample? This can be answered considering the dynamics in the process of domain switching, and the semi-conductivity of ferroelectrics.

At the first stage of the switching process there is a head-to-head interface at the

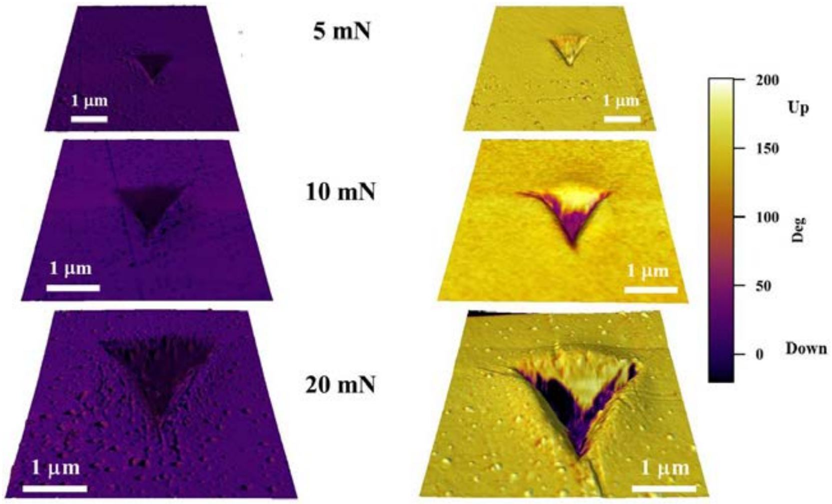

Figure 3.6: *3D plot of topography with the superimposed PFM image of a small area around the indentations in at 5 mN, 10 mN and 20 mN in (a), (c) (e) downward and (b), (d) (f) upward polarization, respectively, showing the switching at (d) 10 mN and (f) 20mN in the upward domains due to flexoelectric effects.*

tip of the propagating needle domain. The bound charges at that interface are initially unscreened, giving rise to a large depolarization field that fights against the antiparallel polarization and thus impairs the growth of the incipient domain. According to the charge – injection model[21-22] developed by Lou and co-workers, screening (and thus switching) becomes possible thanks to the incorporation of free charges coming from the electrodes or defects of the material. It is also known that this depolarization field, related with the electrostatic energy, depends on the conductivity of the material, as Mitsui and Furuichi proposed.[23]It is therefore reasonable hypothesise that domain switching only happens in PPLN and not in SLN because, as explained above, it has a higher density of defects and thus of free charge toscreen the depolarization field at the tip of the incipient domain. In order to confirm that the SLN and PPLN samples had different conductivity, measurements of impedance as a function of frequency were performed in both crystals. From figure 3.7, it can be observed that the impedance obtained for SLN was around one order of magnitude higher than that obtained for PPLN, i.e. the PPLN was more conductive than SLN, consistent with our proposed explanation of why flexoelectric switching occurred in PPLN and not in SLN.

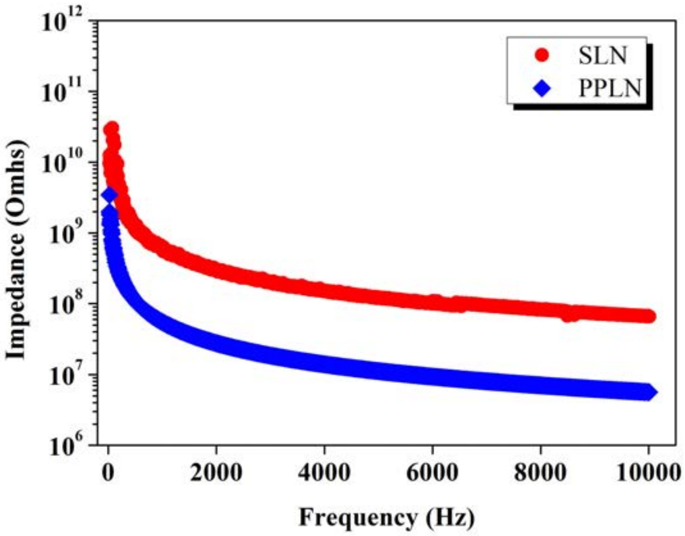

Figure 3.7: *Frequency dependence of the impedance of PPLN and SLN single crystals.*

References

1. Kogan, S. *Phys. Solid State* **5**, 2069-2079 (1964).

2. Tagantsev, A. K. *Phys. Rev. B* **34**, 5883 (1986).

3. Zubko, P., Catalán, G. & Tagantsev, A.K. *Annu. Rev. Mater. Res.* **43**: 387 – 421 (2013).

4. Lakes, R. S. & Benedict, R.L. *Int. J. Engng Sci.* **29**, 1161 (1982).

5. Lu, H., Bark, C. –W., Esque de los Ojos, D., Alcalá, J., Eom, C. B., Catalan, G. & Gruverman, A. *Science* **336**, 59 (2012).

6. Abdollahi, A., Peco, C., Millán, D., Arroyo, M., Catalán, G. & Arias, I. *Phys. Rev. B* **92**, 094101 (2015).

7. Zhou, H., Pei, Y., Li, F., Luo, H. & Fang, D. *Appl. Phys. Lett.* **104**, 061904 (2014).

8. Devonshire, A.F. *Phil. Mag* **40**, 1040 (1949).

9. Sharma, N. D. , Landis C. M., and Sharma P. *J. Appl. Phys.***108**, 024304 (2010)

10. Majdoub, M., Sharma, P. & Çağin, T. *Phys. Rev B* **78**, 121407 (2008).

11. Gharbi, M., Sun, Z. H., Sharma, P. & White, K. *Appl. Phys. Lett.* **95**, 142901 (2009).

12. Robinson, C.R., White, K. W.& Sharma, P. *Appl. Phys. Lett.* **101**, 122901 (2012).

13. Reece, M.J. & Guiu, F. *Philosophical Magazine A* **82**, 1: 29-38 (2002).

14. Weis, R.S. & Gaylord, T.K. *Appl. Phys. A* **37**, 191 – 203 (1985).

15. Kim, S., Gopalan, V., Kitamura, K.& Furukawa. Y. *J. Appl. Phys* **90**, 2949 (2001).

16. Gopalan, V., Dierolf, V. & Scrymgeour, D.A. *Annu. Rev. Mater. Res.* **37**, 449 – 489 (2007).

17. Pharr, G.M. *Mater. Sci. Eng. A* **253**, 151-159 (1998).

18. Cheng, Y. –T & Cheng, C. –M. *Appl. Phys. Lett.* **73**, 614 – 616 (1998).

19. Oliver, W.C. & Pharr, G.M. *J. Mater. Res.* **7**, 1564 – 1583 (1992).

20. Fisher – Cripps, A.C. *Nanoindentation.* 3rd Ed. Springer – Verlag, New York (2002).

21. Lou, X.J., Zhang, M., Redfern, S.A.T.& Scott, J.F. *Phys. Rev. Lett.* **97**, 177601 (2006).

22. Lou, X.J., Zhang, M., Redfern, S.A.T. & Scott, J.F. *Phys. Rev. B.* **75**, 224104 (2007).

23. Mitsui, T. & Furuichi, J. Phys. Rev. 90, 2 (1953).

CHAPTER 4

Nanomechanics: measuring flexoelectricity from nanoindentation

---

Having demonstrated experimentally that flexoelectricity induces asymmetry in the energy cost and in the mechanical response of ferroelectric materials, an interesting question then arises: is it possible to measure the flexoelectric coefficient of ferroelectrics based on their mechanical response?

This question is relevant because flexocoupling coefficients measured in ferroelectrics using the standard beam-bending method[1-2] can exceed the theoretical upper limit by several orders of magnitude;[3] our own beam-bending measurements of z-cut SLN, for example, yielded unrealistic values of 30000V, and similarly excessive flexoelectricity has also been reported for the ferroelectric phase of BaTiO3. [4]

In this chapter it will be showed that from the equation of the free energy of ferroelectrics is possible to obtained a analytical expression to calculate the flexocoupling coefficient, and using the values obtained in chapter 3, it will be estimated the value for $LiNbO_3$.

4.1 Calculation of the flexoelectric coefficient

Equation (3.4) in section 3.2 suggests that might be possible to obtain an estimation of the flexocoupling coefficient from the difference between the mechanical responses of opposite polarity. Assuming $P_k^+ + P_k^- \equiv P_k$, equation 3.4 can be re-written as

$$\Delta G = -2 \int f_{ijkl} P_k \frac{\partial \varepsilon_{ij}}{\partial x_l} dV \tag{4.1}$$

This equation states that the difference between the free energies of the two polarities is directly proportional to the flexoelectric tensor, with the proportionality being given by the integral of the polarization times the strain gradient. So, in principle, if we can calculate this integral and measure the free energy difference, the flexoelectric coefficients can be extracted. For a simple order-of-magnitude estimation, we consider a pseudocubic medium where the only non-zero independent flexoelectric coefficients f_{ijkl} are the longitudinal f_{11} and transversal f_{12} (Voigt notation is used)[5] so that the right-hand side of equation 4.1 can be expanded as

$$\begin{aligned} \Delta G = -2 \int \Bigg[f_{11} \left(P_1 \frac{\partial \varepsilon_{11}}{\partial x_1} + P_2 \frac{\partial \varepsilon_{22}}{\partial x_2} + P_3 \frac{\partial \varepsilon_{33}}{\partial x_3} \right) & \\ + f_{12} \Bigg(P_1 \frac{\partial \varepsilon_{22}}{\partial x_1} + P_1 \frac{\partial \varepsilon_{33}}{\partial x_1} + P_2 \frac{\partial \varepsilon_{11}}{\partial x_2} & \\ + P_2 \frac{\partial \varepsilon_{33}}{\partial x_2} + P_3 \frac{\partial \varepsilon_{11}}{\partial x_3} + P_3 \frac{\partial \varepsilon_{22}}{\partial x_3} \Bigg) \Bigg] dV & \end{aligned} \tag{4.2}$$

We further simplify by assuming that $f_{11} = f_{12} = f$, and consider x_3 as the uniaxial direction of the spontaneous polarization, i.e. $P_1 = P_2 = 0$, and $P_3 \equiv P_0$. Using the simplified Hook's law, $\varepsilon = \sigma / E$, equation 4.2 becomes

$$\Delta G = -\frac{2 f P_0}{E} \int \left(\frac{\partial \sigma_{11}}{x_3} + \frac{\partial \sigma_{22}}{x_3} + \frac{\partial \sigma_{33}}{x_3} \right) dV \tag{4.3}$$

where P_0 is the spontaneous polarization of LiNbO3.

Following an idealized model of indentation,[6] the surface of the indenter is assumed to be encased in a semi-cylindrical or hemispherical core where there is a hydrostatic stress, which is given by

$$\hat{\sigma} = \frac{\sigma_{11} + \sigma_{22} + \sigma_{33}}{3} \tag{4.4}$$

The volume integral can therefore be reduced over the surface, and equation 4.4 is given by

$$\Delta G = -\frac{6fP_0}{E} \iint \hat{\sigma} dx_1 dx_2 \tag{4.5}$$

The stress is given by

$$\hat{\sigma} = -\frac{F}{A} \tag{4.6}$$

with F being the indentation force and A the projected area. Equation 4.7 can therefore be written as

$$\Delta F = \frac{6fFP_0}{E} \tag{4.7}$$

And, thus, the flexocoupling coefficient f is obtained as

$$f = \frac{1}{6} \frac{E\Delta G}{P_0 F} \tag{4.8}$$

where P_0 is the spontaneous polarization (0.8 C/m^2 for $LiNbO_3$ [7]), F is the maximum indentation load and $\hat{E}$ is the average of the elastic modulus measured for the up- and down-polarized states.

Meanwhile, the energy difference ΔG can be calculated from the difference in the elastic energies of both polar states measured by the nanoindenter, which is $\Delta G = U_e^+$ - U_e^- . Using the values obtained experimentally at 7 mN, and the equation 4.8, the calculated flexocoupling coefficient f is 54 ± 4 V for SLN and 40 ± 5V for PPLN.

The calculated flexocoupling coefficients are somewhat larger than might be expected from application of the Kogan-Tagantsev criterion, whereby f is of the order of 10V or less. The result is nevertheless comparable to the value of paraelectric $BaTiO_3$ (f=20V).[4] The agreement is remarkable considering the fairly crude approximations made in order to obtain an analytical expression (e.g., actual indentations are not spherical). The result is particularly good, considering that our material was in the ferroelectric phase, where additional contributions from piezoelectricity can be expected.[4, 8-9] The mechanical estimate represents a noticeable improvement with respect to the classical quantification of flexoelectricity using the beam-bending method [1-2] where our own measurements for the same crystals yielded, as mentioned, an unrealistically high value of the flexocoupling coefficient.

References

1. Cross L. E. *J. Mater. Sci.* **41**, 53-63 (2006).
2. Ma W. and Cross L. E. *Appl. Phys. Lett.* **88**, 232902 (2006).
3. Zubko, P., Catalán, G. & Tagantsev, A.K. *Annu. Rev. Mater. Res.* **43**: 387 – 421 (2013).
4. Narvaez, J., Saremi, S., Hong, J., Stengel, M. & Catalan, G. *Phys. Rev. Lett.* **115**, 037601 (2015).
5. Shu, L., Wei, X., Pang, T., Yao, X. & Wang, C. *J Appl Phys* **110**, 104106 (2011).
6. Johnson, K. L. *J Mech Phys Solids* **18**, 115 – 126 (1970).
7. Kim, S., Gopalan, V., Kitamura, K. & Furukawa. Y. *J. Appl. Phys* **90**, 2949 (2001).
8. Biancoli, A., Fancher, C.M., Jones, J.L., & Damjanovic, D. *Nat. Mater.* **14**, 224–229 (2015).
9. Hana P. *Ferroelectrics* **351**, 196-203 (2007).

CHAPTER 5

Cracking flexoelectricity

Crack propagation causes materials to break, so understanding it is vital for materials engineering. In addition, controlled cracking has been proposed as a possible mechanism for nanodevice patterning,[1] making the harnessing of crack propagation a constructive pursuit. In piezoelectric and ferroelectric materials, fracture mechanics is also functionally important because fatigue due to microcracking affects their response in electromechanical transducers.[2-3] Understanding the fracture behaviour of ferroelectrics is therefore important in many ways: it is essential for improving their mechanical endurance and fatigue resistance, and it may be useful also as a strategy for their nanopatterning.

But besides these features, there is another singular aspect that is relevant for this thesis: the front of a crack tip contains the highest strain gradient that any material can withstand, and it is therefore a likely source of flexoelectric effects. This chapter presents the research of the effects of flexoelectricity on crack propagation of uniaxial ferroelectrics. It will be demonstrated experimentally that flexoelectricity enables a diode-like fracture behaviour in ferroelectrics, whereby crack propagation can be facilitated or impaired according to the sign of the ferroelectric polarization. Additionality, the flexoelectric domain switching zone around the crack tip will be estimated using an analytical model for the flexoelectric field at the front of a crack tip. As will be argued, crack-induced flexoelectric switching is a contributor to the toughening of ferroelectrics with polarization antiparallel to the crack.

5.1 Crack propagation with respect to the polarization

Most studies related to fracture and crack propagation in ferroelectrics are focused on the influence of stress and electric field in fracture toughness anisotropy, i.e., comparing crack propagation parallel to the polarization against propagation perpendicular to it. For example, it has been demonstrated, through indentation tests on the base of Vickers tips (with square pyramidal geometry), that under the action of only a mechanical load, fracture toughness of the crack along the poling direction is relatively higher than the fracture toughness of the crack perpendicular to the poling direction of the material [4, 5, 6]. In addition, it has been shown that, in unpoled materials, application of an external electric field during tests promotes crack propagation perpendicular to the applied electric field, so that fracture toughness anisotropy is increased by voltage [7, 8, 9, 10]. However, this chapter is not concerned with anisotropy (difference between different directions) but with asymmetry (difference between different polarities along the same direction). While the former is a predictable consequence of the anisotropy of the crystal lattice, the latter can only be understood in the presence of flexoelectricity.

Recently, a theoretical work [11] demonstrated that, since the local deformation at the crack-tip generates a flexoelectric field, and thus a flexoelectric polarization, the fracture toughness in ferroelectric thin films must be asymmetric with respect to the sign of the ferroelectric polarization, for the same reasons discussed in chapter 3. Motivated by this prediction, we have studied experimentally the behavior of crack propagation in ferroelectrics with in-plane polarization.

5.1.1 Experiment

The material used for this study was a poled Rb-doped $KTiOPO_4$ (RKTP) single crystal, with the ferroelectric polarization oriented in-plane, and containing two domains of antiparallel orientation.[i] This material was chosen because it is a uniaxial ferroelectric, and thus ferroelastic effects can be excluded. Furthermore, using a poled material, with opposite polarization directions ensures that geometrical effects, such as a slight tilt or miscut of the crystal surface, do not affect the results.

---

[i] The sample was kindly provided by Dra. Carlota Canalias at KTH-Albanova, Sweden

In order to induce controled cracking, Vickers Indentation Tests were performed by applying sets of 200mN and 300mN loads, with the orientation of the indenter being such that two of its four corners were parallel to the polar axis and the other two perpendicular.

In order to collect statistically meaningful results, 30 indents for each force (15 for each domain polarity) were performed, with each indent generating four orthogonal cracks along the parallel, antiparallel and perpendicular directions. In total, therefore, 240 cracks were analysed. The radial crack lengths were measured with an optical microscope immediately after indentation. A sketch of the experiment is in Figure 5.1(a), and two indentation examples can be seen in Figure 5.1(b) and 5.1(c). After measuring the length of the cracks "l", the length asymmetry along the polar axis was calculated for each indentation. To verify that the results did not include geometrical artefacts, the asymmetry in the direction perpendicular to the polar direction, which in theory should be null, was also measured.

Similar to the previous chapter, the asymmetry is defined as:

$$\%Asym \equiv 100\frac{l^+ - l^-}{\langle l \rangle} \tag{5.1}$$

where \$l^+$" is the crack length parallel to the polarization, and \$l^-$" is the crack length antiparallel to the polarization (up or down in the plan-view photos). For cracks perpendicular to the poling direction, + and – designate right and left directions, respectively, in the planar-view photos, and the average crack length is $\langle l \rangle \equiv \frac{l^+ + l^-}{2}$. Positive (negative) asymmetry indicates a longer (shorter) crack length in the parallel direction than the average. Zero asymmetry means both cracks (parallel and antiparallel) have the same length.

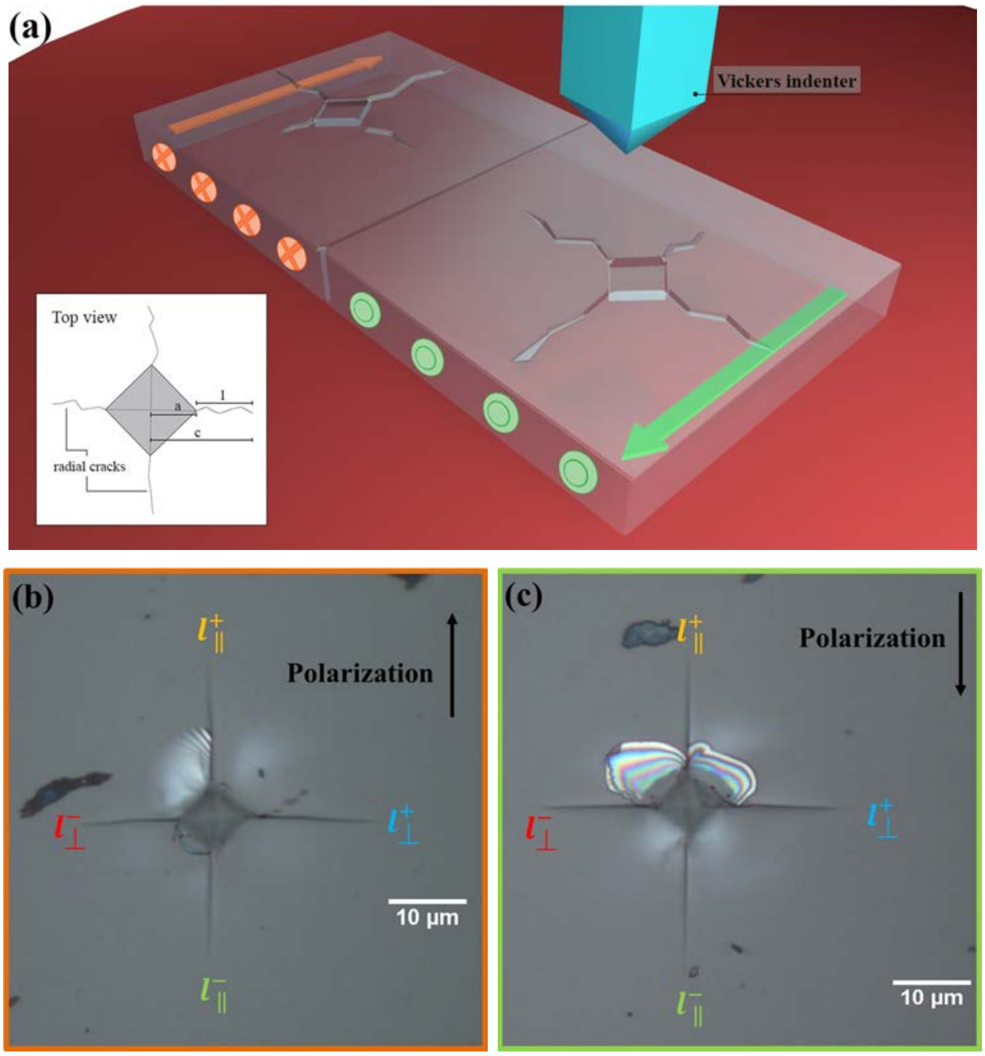
(a)
Vickers indenter
Top view
l
a
c
radial cracks
(b)
$l_{\parallel}^{+}$
Polarization
$l_{\perp}^{-}$
$l_{\perp}^{+}$
10 μm
$l_{\parallel}^{-}$
(c)
$l_{\parallel}^{+}$
Polarization
$l_{\perp}^{-}$
$l_{\perp}^{+}$
10 μm
$l_{\parallel}^{-}$

Figure 5.1: *(a) Schematic of the Vickers Indentation test showing the top view of typical radial crack propagation for indentation fracture toughness measurement with corresponding crack and diagonal lengths. Optical micrographs of Vickers indent in RKTP showing the radial crack propagation for (b) up and (c) down polarization.*

5.2 Crack length behaviour

As a reference, Figure 5.1(a) shows the asymmetry of the cracks perpendicular to the polar axis. For these, as expected, there is no asymmetry within statistical error. This lack of perpendicular asymmetry provides a safety check for the robustness of the experiment, and a suitable background for comparison. In contrast to the perpendicular cracks, crack length along the poling direction is clearly asymmetric, see Figure 5.1(b): for the domains P^+ a positive asymmetry is measured, and the asymmetry is exactly reversed for the domains P^-. In other words, the crack length parallel to the polarization is always greater than the crack length antiparallel to the polarization, irrespective of the polarity of the domain. Since all indentations are performed under the exact same geometrical conditions, the fact that the asymmetry is reversed when the polarization is inverted implies that the origin of the asymmetry cannot be a geometrical artifact. In addition, differences in surface adsorbates or near-surface defects can also be excluded; even if such differences did exist (and none should be expected given that the polarization is in-plane), each pair of cracks is generated from the same spot and thus experiences the same conditions. Thus, by experimental design, surface conditions are inherently unable to cause crack length asymmetry. The asymmetry in crack propagation is therefore intrinsic and linked to the in-plane polarity.

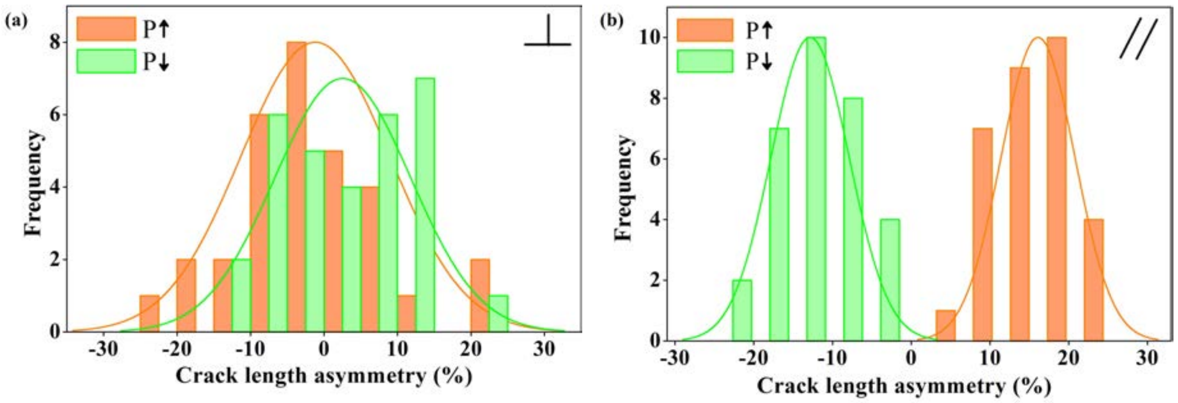

Figure 5.2: *Figure 4.2: Crack length asymmetry (a) perpendicular and (b) parallel to the polar axis.*

5.3 Mechanical properties behaviour

The asymmetry of crack length can be used to quantify the asymmetry in fracture toughness, which measures the stress intensity required for creating a crack [12]. Fracture toughness is given by[13]

$$K_{IC} = 0.016 * \left(\frac{E}{H}\right)^{1/2} \left(\frac{F}{c^{3/2}}\right), H = \frac{F}{2a^2} \tag{5.2}$$

where E is the Young Modulus, H the Vickers hardness, F the indent load, c is the distance from the center of the indentation impression to the tip of the crack, and 2a is the diagonal of the indent (see inset in Figure 5.1a). Using the values obtained from our tests, K_{IC} was obtained for each crack, and then using the expression 5.1, the asymmetries were calculated.

Figure 5.3(a) and 5.3(b) show the asymmetry for the perpendicular and parallel directions, respectively. As expected, there is only asymmetry along the polar axis, i.e. when ferroelectric and flexoelectric polarizations are parallel (crack propagating in the same direction as the ferroelectric polarization), or antiparallel (crack propagating in the opposite direction of the ferroelectric polarization). The average value of the fracture toughness for cracks parallel to the polarization was $\sim 0.19 \pm 0.02$ MPa $m^{1/2}$, whereas for the ones antiparallel to the polarization it was $\sim 0.23 \pm 0.03$ MPa$m^{1/2}$. In other words, in ferroelectric materials, fracture toughness is enhanced (thus yielding to shorter cracks) by 20% when flexoelectricity and ferroelectricity are antiparallel compared to when they are parallel. Conversely, the mechanical properties measured perpendicular to the crystal (Stiffness, Young Modulus, and Hardness) should be symmetric, because they are orthogonal to the ferroelectric polarization. In order to verify this aspect, we checked the other mechanical properties and the energies (plastic and elastic) obtained from the tests. The mean values for each property were calculated for each polarity, and the asymmetry

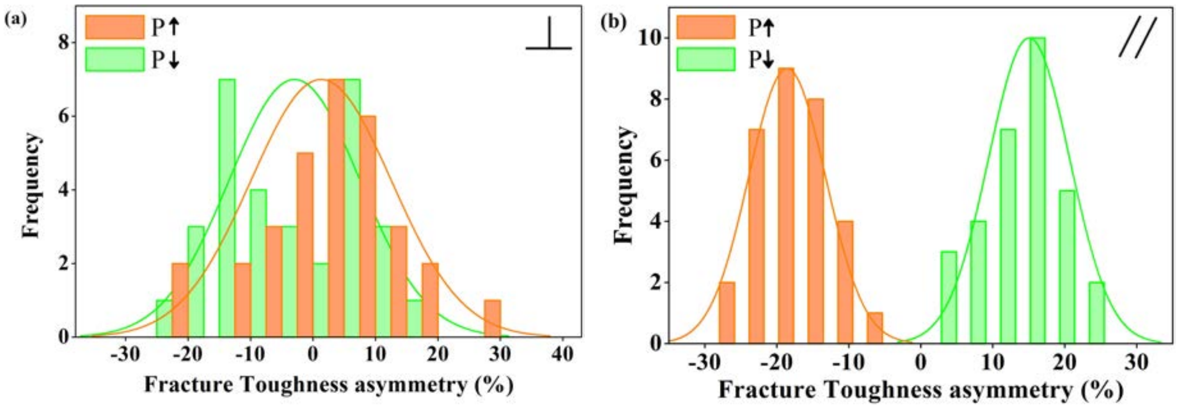

Figure 5.3: *Figure 4.3: Facture toughness asymmetry (a) perpendicular and (b) parallel to the polar axis*

was calculated using the equation 5.1.

Table 5.1 and 5.2 contain the values obtained for all the cracks (indentation loads of 200mN and 300mN, respectively). In all cases, the asymmetry essentially zero within the statistical variance . These results provide further evidence that flexoelectricity is the origin of the asymmetry in the in-shown figure 5.3.

This asymmetry can be explained on the basis of the interplay between flexoelectricity and ferroelectricity [11, 14] described in Chapter 3. The local deformation at the tip of the crack generates a flexoelectric polarization.[11] Depending on whether this flexoelectric polarization is parallel or antiparallel to the ferroelectric polarization, it will result in different electrostatic energy costs for crack propagation. A higher depolarization energy means a higher energy cost for crack propagation, and thus a shorter crack.

Property	P^+ (↑)	P^- (↓)	Asym (%)
Hardness (GPa)	7.3 ± 0.8	7.4 ± 0.7	-1 ± 1
Stiffness ($mN/\mu m$)	590 ± 8	605 ± 9	-2 ± 1
Plastic energy nJ	45 ± 2	46 ± 2	-2 ± 1
Elastic energy nJ	39 ± 1	38 ± 1	-2 ± 1

Table 5.1: *Mechanical properties and energies costs as function of the polarity for RKTP at 200 mN.*

Property	P^+ (↑)	P^- (↓)	Asym (%)
Hardness (GPa)	7.8 ± 0.7	7.9 ± 0.4	-1 ± 1
Stiffness ($mN/\mu m$)	710 ± 16	700 ± 19	2 ± 1
Plastic energy nJ	84 ± 2	86 ± 2	-2 ± 1
Elastic energy nJ	73 ± 2	74 ± 1	-2 ± 1

Table 5.2: *Mechanical properties and energies costs as function of the polarity for RKTP at 300 mN.*

In addition, the flexoelectric field near the tip of the crack may be large enough to cause local switching of the polarization,[15-16] thus providing an additional path for energy dissipation that further reduces the available energy for mechanical fracture. This idea is examined in more detail in the following section.

5.4 Domain Switching

As mentioned in the previous section, if the flexoelectric field near the tip of the crack is large enough, there is the chance that it can cause local switching of the polarization,[15-16] thus providing an additional path for energy dissipation. This process is known as switching-induced toughening,[17, 18, 19] and the size of the switching region can be calculated by comparing the electrostatic energy cost of switching (switched polarization multiplied by coercive field) against the mechanical and electromechanical energy provided by the crack.[17] Considering a generic ferroelectric, and adding a flexoelectric term to the energy balance, switching should occur when:

$$f_{ijkl} P_i \varepsilon_{j,kl} + \sigma_{ij} \Delta\varepsilon_{ij} + E_i \Delta P_i \geq 2 P_s E_c \tag{5.3}$$

where f_{ijkl} is the flexocoupling tensor, Pi is the induced polarization, $\varepsilon_{j,kl}$ is the strain gradient, $\Delta\varepsilon_{ij}$ and $\Delta\Pi$ are the changes in the spontaneous strain and spontaneous polarization during the switching, respectively; Ps is the magnitude of the spontaneous polarization; and Ec the coercive electric field. Since the experiments were performed in absence of an external electric field, we can discard the third term, and we can also discard the second because in a uniaxial ferroelectric there is no ferroelastic switching and thus no change in spontaneous strain, i.e. $\Delta\varepsilon_{ij} = 0$.[18] The condition for switching thus simplifies to

$$f_{ijkl} \varepsilon_{j,kl} \geq 2 E_c \tag{5.4}$$

In other words, switching happens when the flexoelectric field (left side of the equation) exceeds the coercive field (right side term). The effective flexoelectric field[20] is given by

$$E_l = f_{ijkl} \frac{\partial \varepsilon_{ij}}{\partial x_k} \tag{5.5}$$

where f_{ijkl} is the strain gradient – electric field coupling coefficient (flexocoupling coefficient), ε_{ij} is the strain, and x_j the position coordinate. The flexoelectric field components for a pseudocubic two dimensional (2D) case [21], which is the one described above (crack propagating along a surface), are given by

$$E_1 = f_{11}\frac{\partial\varepsilon_{11}}{\partial x_1} + f_{12}\frac{\partial\varepsilon_{22}}{\partial x_1} + f_{44}\frac{\partial\varepsilon_{12}}{\partial x_1} \tag{5.6}$$

$$E_2 = f_{22}\frac{\partial\varepsilon_{22}}{\partial x_2} + f_{21}\frac{\partial\varepsilon_{11}}{\partial x_2} + f_{44}\frac{\partial\varepsilon_{12}}{\partial x_2} \tag{5.7}$$

where f_{11}, f_{12} and f_{44} are the longitudinal, transversal and shear components of the flexocoupling coefficient. In order to obtain an order-of-magnitude estimate of the switched region, we have used the expression 5.6, and simplified the problem as usual by neglecting the shear strain gradient and considering only longitudinal and transverse components. Besides, we assumed flexocoupling coefficients of the order of f = 10V, as observed for ceramics.[22-23] With these simplifications, switching should occur when:

$$\left(\frac{\partial\varepsilon_{22}}{\partial x_1} + \frac{\partial\varepsilon_{11}}{\partial x_1}\right) \geq \frac{2E_c}{f} \tag{5.8}$$

Considering the coercive field of RKTP ($E_c = 3.7x10^6\ Vm^{-1}$), we thus calculate that a strain gradient of $7.4x10^5\ m^{-1}$ is required in theory to induce switching in RKTP. Next we use finite element analysis to map the theoretical strain gradient field around a crack tip and determine if it is big enough to exceed the coercive field, and, if so, what is the expected size of the flexoelectrically switched region.

The strain field[24] in any linear elastic cracked material is given by

$$\varepsilon_{ij}^{el} = \frac{1+\nu}{E}\sigma_{ij} - 3\frac{\nu}{E}\sigma_m\delta_{ij} \tag{5.9}$$

where σ_{ij} is the stress applied to the crack in each direction, and its expression depends on the propagation modes; σ_m is the average stress, E is the Young's Modulus, and ν is the Poisson ratio of the material.

As described in the introduction, three different types of cracks exist, which are defined by the propagation mode of crack. Focusing on crack mode I (tensile loading), which is the one generated with the tests, the stress fields in this type of crack are given by the following equations :

$$\sigma_{11} = \frac{K_I}{E\sqrt{2\pi r}} cos\frac{\theta}{2}\left(1 - sin\frac{\theta}{2} sin\frac{3\theta}{2}\right) \tag{5.10}$$

$$\sigma_{22} = \frac{K_I}{E\sqrt{2\pi r}} cos\frac{\theta}{2}\left(1 + sin\frac{\theta}{2} sin\frac{3\theta}{2}\right) \tag{5.11}$$

$$\tau_{12} = \frac{K_I}{E\sqrt{2\pi r}} cos\frac{\theta}{2} sin\frac{\theta}{2} cos\frac{3\theta}{2} \tag{5.12}$$

where K_I is the stress intensity factor (fracture toughness for this calculation).

Substituting equations 5.10, 5.11 and 5.12 in equation 5.9, it is possible to obtain the expressions that describe the strain field around a crack tip of crack mode I:

$$\varepsilon^{el}_{11} = \frac{K_I}{E\sqrt{2\pi r}} \cos\frac{\theta}{2}\left((1 - \nu - sin\frac{\theta}{2}\sin\frac{3\theta}{2}(1+\nu)\right) \tag{5.13}$$

$$\varepsilon^{el}_{22} = \frac{K_I}{E\sqrt{2\pi r}} \cos\frac{\theta}{2}\left((1 + \nu - sin\frac{\theta}{2}\sin\frac{3\theta}{2}(1+\nu)\right) \tag{5.14}$$

$$\varepsilon^{el}_{12} = \frac{1+\nu}{E}\frac{K_I}{\sqrt{2\pi r}} \cos\frac{\theta}{2}\sin\frac{\theta}{2}\cos\frac{3\theta}{2} \tag{5.15}$$

From these expressions, using the values obtained from the tests, and we can map the theoretical strain field analytically and, using Mathematica,[25] compute and map the strain gradient around the crack tip .

The calculated 2D strain field and strain gradient map around a crack tip in RKTP is plotted in Figure 5.4. The black line marks the distance from the crack tip within which there is in theory enough flexoelectricity to induce local switching of the polarization. We see that, as the crack propagates, it can switch the polarization in a volume of $\sim$ 5 nm

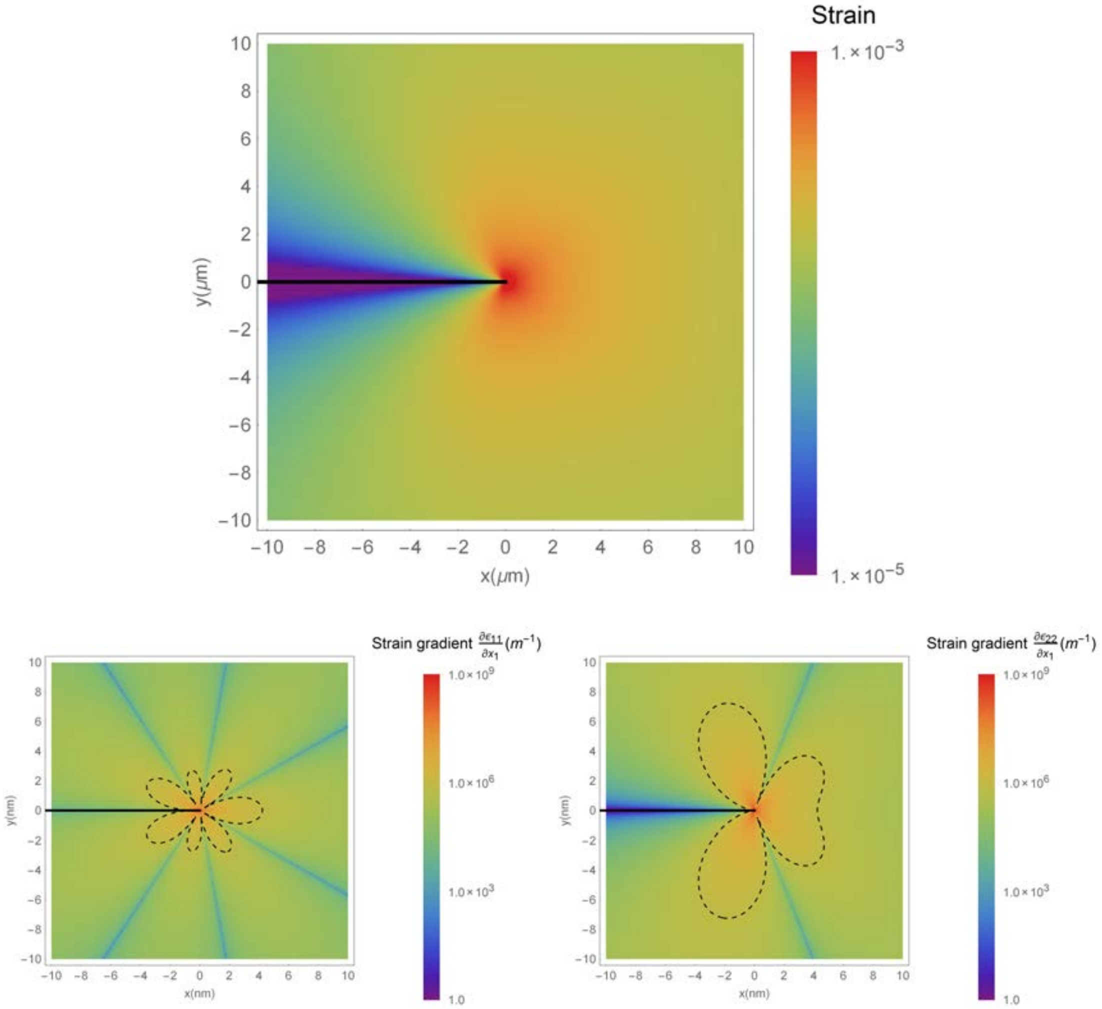

Figure 5.4: *Calculated distribution of the (a) strain field, and strain gradient components (b) longitudinal, (c) transversal around the apex of a crack in RKTP. The black line marks the region where the field is strong enough to be able to induce local switching of the polarization*

around the crack tip, thus dissipating energy and therefore reducing the maximum length that the crack can reach. The cracks were examined by PFM to seek evidence of such switched nano-regions, but none was found. The calculated size of the domains is in fact so small as to be at (or beyond) the resolution limit of PFM, and they are also close to the limit for thermodynamic stability of a switched domain embedded in a non-switched matrix. It might be that the switched region is there but is too small for the PFM, or it perhaps it is not there at all due to back-switching.

References

1. K. H. Nam, I. H. Park & S. H. Ko. *Nature* **485**, 221–224 (2012).
2. S. Kim & Q. Jiang. *Smart Mater. Struct.* **5** 321 (1996).
3. J. Shieh, J. E. Huber & N.A. Fleck. *J. Eur. Ceram. Soc.* **26**, 95 – 109 (2006).
4. G.G. Pisarenko, V. M. Chushko & S.P. Kovalev. *J. Am. Ceram. Soc.* **68(5)**, 259-265 (1985).
5. K. Mehta & A.V. Virkar. *J. Am. Ceram. Soc.* **73(3)**, 567-574 (1990).
6. J.M. Calderon-Moreno, F. Guiu, M. Meredith & M.J. Reece. *Mater. Sci Eng A.* **234**, 1062-1066 (1997).
7. T. Yamamoto, H. Igarashi & K. Okazaki. *Ferroelectrics* **50**, 273-278 (1983).
8. A.G. Tobin & Y.E Pak. *Proc. SPIE Smart Struct. Mater* **1916**, 78-86 (1993).
9. C.S. Lynch. *Acta mater* **46(2)**, 599-608 (1998).
10. G.A. Schneider & V. Heyer. *J. Eur. Ceram. Soc.* **19**, 1299-1306 (1999).
11. A. Abdollahi, C. Peco, D. Millán, M. Arroyo, G. Catalan & I. Arias. *Phys. Rev. B* **92**, 094101 (2015).
12. A.C. Fischer – Cripps. *Introduction to contact mechanics.* Springer press, second edition (2007).
13. G.R. Anstis, P. Chantikil, B.R. Lawn & D.B. Marshall. *J. Amer. Ceram. Soc.* **62**, 347-359 (1979).
14. Zhou, H., Pei, Y., Li, F., Luo, H. & Fang, D. *Appl. Phys. Lett.* **104**, 061904 (2014).
15. H. Lu, C. –W. Bark, D. Esque de los Ojos, J. Alcalá, C. B. Eom, G. Catalán & A. Gruverman. *Science* **336**, 59 (2012).

16. J. Ocenásek, H. Lu, C. W. Bark, C. B. Eom, J. Alcalá, G. Catalan, A. Gruverman, *Phys. Rev. B* **92**, 035417 (2015).

17. S.C. Hwang, C.S. Lynch & R.M. McMeeking. *Acta Metall. Mater.* **43**: 2073 – 2084 (1995).

18. X. Zeng & R.K.N.D Rajapakse. *Smart Mater. Struct* **10**, 203 – 211 (2001).

19. G.A. Schneider. *Annu. Rev. Mater. Res.* **37**: 491 – 538 (2007).

20. W. Ma. *Phys. Stat. Sol. (b)* **245**, 761-768 (2008).

21. R. Ahluwalia, A.K. Tagantsev, P. Yudin, N. Setter, N. Ng & D.J. Srolovitz. *Phys. Rev. B.* **89**: 174105 (2014).

22. P. Zubko, G. Catalan & A.K. Tagantsev. *Annu. Rev. Mater. Res.* **43**: 387 – 421 (2013).

23. J. Narvaez, S. Saremi, J. Hong, M. Stengel, G. Catalan. *Phys. Rev. Lett.* **115**, 037601 (2015).

24. B. Lawn. *Fracture of brittle solids* (Cambridge University Press, Second Edi., 1993).

25. Wolfram Research, Inc. *Mathematica*, Version 10.2, Champaign, IL (2016).

CHAPTER 6

Mechanical reading of polarity

The asymmetric behaviour of the mechanical properties in ferroelectrics, explained in chapter 3 represents a paradigm shift. In terms of solid state mechanics, asymmetric fracture is a fundamentally new phenomenon. In terms of functionality, it enables hitherto symmetry-forbidden device concepts, such as smart coatings with switchable mechanical response. It also opens up the fascinating possibility of detecting the polar state of a ferroelectric memory just by mechanical means. The potential usefulness of such a concept is that reading can thus be achieved without the need of electrodes, and without the need to apply any voltage to the ferroelectric, thus bypassing leakage current problems. Chapter 3 showed that nanoindentation could be used for detecting polarity, but indentation is not a practical reading mechanism: it is, by definition, a destructive technique. The present chapter will extend the concept of mechanical reading to a non-destructive method with nanoscopic resolution.

The technique investigated is contact resonance frequency tracking by atomic force microscopy. This technique allowed the detection of small shifts in mechanical resonance frequency due to the polarity-dependent contact stiffness. The present chapter will describe the concept of mechanical reading, demonstrate that the AFM-base technique works for reading the polarity ferroelectrics, and discuss the dependence of its sensitivity on parameters such as sample thickness and cantilever stiffness.

6.1 Mechanical stiffness in ferroelectric materials

Chapter 3 showed that, under inhomogeneous deformation, the mechanical response of ferroelectrics depends on the sign of the ferroelectric polarization. This mechanical reading concept is explicitly demonstrated in Figure 6.1, which shows how material stiffness, measured by indentation, is a direct proxy for the polarity of the indented domain in a PPLN single crystal: downward-polarized domains have a higher stiffness value than are than upward-polarized ones. In other words, downward polarization is stiffer whereas upward polarization is more flexible.

Although nanoindentation is destructive, stiffness is an elastic property, so in principle it should notbe necessary to punch holes in order to read polarity. The idea is to detect the gradient-induced contrast in polarity-dependent surface stiffness by non-invasive methods and with nanoscopic lateral resolution. These are a necessary (but by no means sufficient) conditions for the concept of mechanical reading to have a chance of being useful for ferroelectric memories.

In order to achieve these goals, we take advantage of the strain gradients generated by the AFM tip to activate the flexoelectric effect. The mechanical contact resonance frequency is monitored through Contact Resonance Frequency (CRF) tracking, making it possible to read the polarity in a non-destructive way.

6.2 Mechanical reading of polarization by CRF

Contact Resonance Frequency (CRF) microscopy is an AFM-based that allows mapping contrasts in a material's surface stiffness in a non-invasive and reversible way, as explained in section 2.3. The main idea is that contact stiffness determines the mechanical resonance frequency, so the polarity-dependent changes in stiffness already demonstrated by nanoindentation (Figure 6.1 above) could in principle be detectable as changes in resonance frequency, with the stiffer down-domains having faster resonance than the softer up-domains. In the past, a similar technique such as Atomic Force Acoustic Microscopy

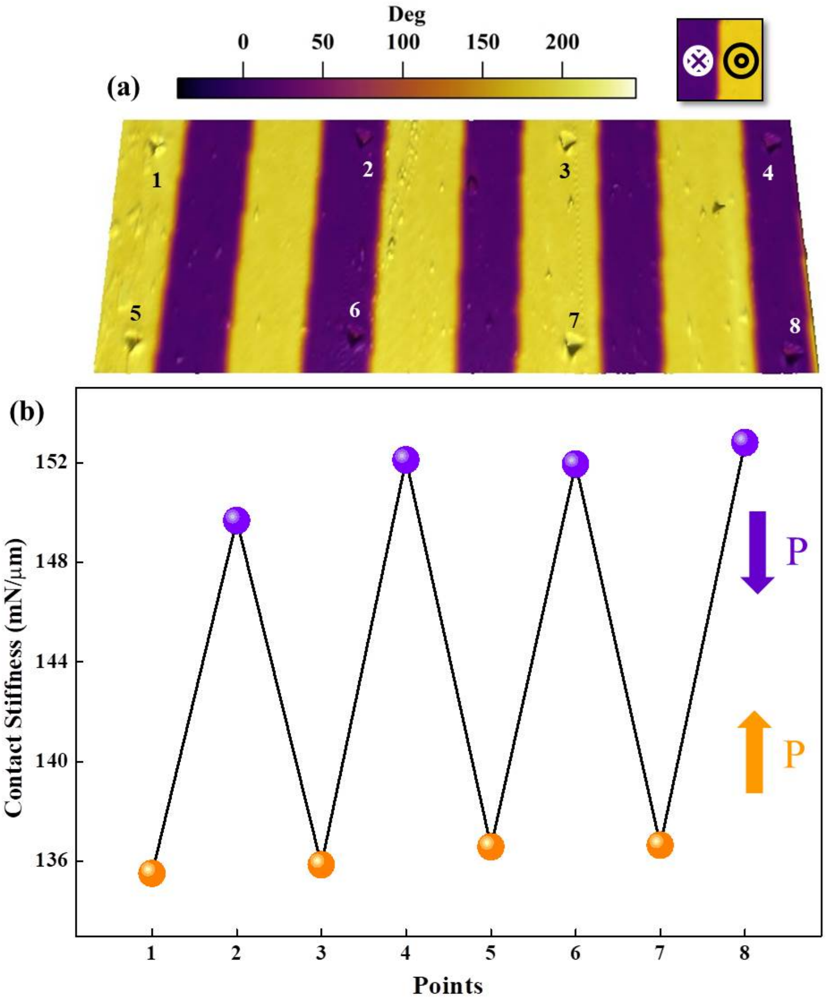

Figure 6.1: *a) 3D plot of topography with superimposed PFM phase image of a few indents performed in PPLN sample at 7 mN. Yellow franges correspond to phase shifts of 180°, related to ferroelectric dipoles with polarization out of plane and pointing up, whereas purple denotes a phase shift of 0°, meaning that polarization is pointing down. b) Contact Stiffness of each indentation number of Figure (a), demonstrating that the relative stiffness is a direct indicator of a polar state, and therefore it is possible to "read" the polarization of a ferroelectric from its mechanical response.*

(AFAM) was successfully used to distinguish mechanical contrast between domains of different ferroelastic orientation;[1, 2, 3] owing to the fact that sample stiffness differs for domains with different spontaneous strain directions. However, it was thought that this technique should be blind with respect to polarization sign. This is because, as discussed before, because in the absence of flexoelectricity, the spontaneous strain and thus the mechanical properties are the same for domains of opposite polarity.

On the other hand, it is known that AFM tips can induce very high and very localized mechanical loads at the nanoscale . Even though the forces delivered by an AFM cantilever are generally small, they are applied over nanometric contact areas, so the effective local pressure (force divided by area) can be large, and thus also the local strain. But due to its characteristic geometry, it has also been demonstrated that under the tip of an AFM, the strain is not homogeneous, resulting in huge but nanoscopically localized strain gradients.[4] In fact, the tip induced strain gradients on a ferroelectric thin layer have been proven to be sufficiently large to mechanically switch the polarization of ferroelectric thin films[5] by the flexoelectric effect. The expectation is that the AFM-induced flexoelectricity also will induce enough asymmetry in the local tip-sample mechanical stiffness to be detected by CRF.

To investigate this possibility, the same PPLN single crystal measured in Chapter 3 was characterized by CRF. The CRF experiments were carried out using an Asylum MFP-3D AFM, with Nanosensors PPP – EFM PtIr coated tips with a k $\sim$ 3 N/m. As explained in section 2.3, this technique is based on the detection of the mechanical resonance frequency of the AFM cantilever, which depends both on the cantilever and on the material that it is contacting. In this case, the mechanical ac excitation signal was applied to the piezo that controls the cantilever. The cantilever was in hard contact with the surface of the ferroelectric, and the resonance frequency was monitored operating in DART mode. As the presence of adsorbates in the sample can play an important and spurious role,[7] measurements were made in a controlled ambient with N_2.

Figure 6.2 show that, contrary to what was believed at the time of the seminal Rabe studies of CRF in ferroelectrics , there is in fact a measurable difference between the contact resonance frequencies of oppositely-polarized domains, with down-polarized domains resonating at higher frequencies (stiffer) than up-polarized ones, in agreement with the nanoindentation results in Figure 6.1 The contact force between the cantilever and the sample was approximately $1.5\mu N$, and the frequency shift observed was$\sim$ 47 Hz.

This result thus further confirms the arguments used to explain the indentation results; inhomogeneous deformation under the AFM tip induces a flexoelectric polarization that

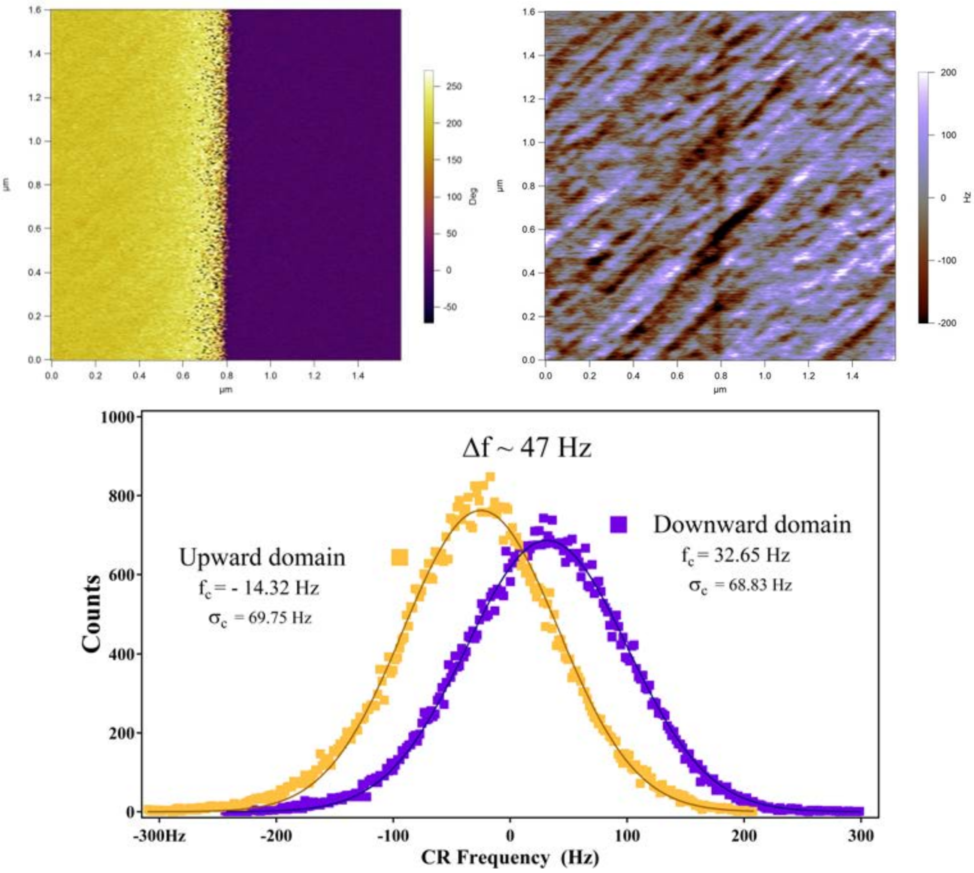

Figure 6.2: *(a)Phase PFM image showing the polarization of the domains in a periodically pooled* $LiNbO_3$ *sample (PPLN), with PhPFM =* 0^o *for domains pointing down and PhPFM =* 180^o *for domains pointing up. (b). Contact resonance frequency mapping of the PPLN surface, the contact resonance frequency is shifted towards higher frequencies for down-polarized domains, meaning they are stiffer, and to lower frequencies for the up-polarized domains, meaning they are softer. (c). Histogram of the CR-AFM image shown in b: the yellow dots correspond to the frequency shift counts in the areas associated to domains pointing up and purple squares to domains pointing down. Black lines are the corresponding Gaussian fittings, with parameters shown in the inset. The total CR frequency contrast among different polarized domains is of about* $\Delta f \sim 47$ *Hz, using a cantilever of* $k \sim 3$ *N/m.*

either adds to or subtracts from the polarization of the ferroelectric domains depending on their ferroelectric sign, resulting in asymmetric energy costs of deformation and thus different stiffness and contact resonance frequency. The result also demonstrates that it is possible to read polarization "by touch" in a non-destructive manner. Next, we look at what factors influence the sensitivity of the technique.

The mechanical resonance of the cantilever in contact with the surface strongly depends on the stiffness of the cantilever, and this in turn depends on the cantilever geometry,[8]

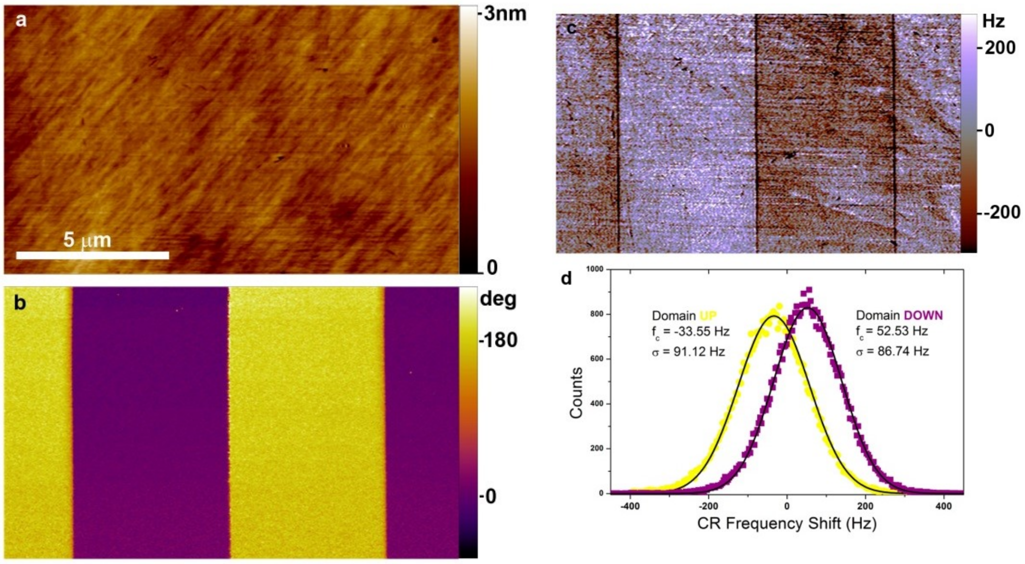

Figure 6.3: *(a) Topography and (b) Phase PFM image showing the polarization of the domains in a periodically pooled* $LiNbO_3$ *sample (PPLN) (c) Contact resonance frequency mapping of the PPLN surface (d) Histogram of the CR-AFM image shown in c: the yellow dots correspond to the frequency shift counts in the areas associated to domains pointing up and purple squares to domains pointing down. Black lines are the corresponding Gaussian fittings, with parameters shown in the inset. The total CR frequency contrast among different polarized domains is of about* $\Delta f \sim$ *86 Hz, using a cantilever of k* $\sim$*48 N/m.*

as explained in Section 2.3. In fact, the key parameter is the stiffness of the cantilever compared to that of the sample. If the cantilever is soft and the sample is rigid (always the case with ferroelectric crystals), most of the oscillation of the cantilever is determined by the elastic constant of the cantilever itself, with the contact point barely moving. In contrast, if the cantilever is rigid and the sample is soft, the contact point will be able to oscillate more, capturing more of the elastic properties of the material. Since we cannot change the crystal, the only way to increase sensitivity is therefore to use stiffer cantilevers. This will also allow the application of stronger strain and thus also strain gradients.

Following this reasoning, experiments were repeated using another cantilever with the same geometry but with a higher elastic constant. The second type of cantilever used was Nanosensors NCL Pt coated tips, with $k \sim 48N/m$, and the contact force applied was about $25\mu N$.

The results shown in Figure 6.3 again show a higher contact resonance frequency for the domains with polarization pointing down. Importantly, the frequency shift obtained in this case was ∼ 86 Hz, (Figure 6.3d). This is twice as much as measured with the softer cantilever. There are at least two reasons for this enhanced frequency shift. First, by pressing harder, the strain gradients generated under the tip of the AFM are higher, thus a larger flexoelectric field is activated, affecting the cooperation - competition dynamic between flexoelectricity and piezoelectricity explained in chapter 3. Second, the enhancement of cantilever's stiffness also promotes the increase of resolution on contact stiffness as we have just discussed, and as also explained in Section 2.3

6.3 Mechanical reading of polarization in thin films: size effect in the mechanical asymmetry

The demonstration of mechanical reading of polarization complements the known ability of mechanical writing of polarization in ferroelectrics by flexoelectricity[4]. The combination of both enables in principle a coherent concept: a full mechanical treatment, read and write, of ferroelectric polarization in ferroelectric thin film memories.

In order to explore this idea, the mechanical reading by CRF was atttempted using thin films instead of single crystals. The material studied was a fully strained thin film of $PbTiO_3$, with a thickness of about 20 nm, grown on a single crystal substrate of $SrTiO_3$, and with a buffer of $SrRuO_3$, with a thickness of about 10 nm, as bottom electrode.[i] Due to the epitaxial strain, the films were fully oriented with the c-axis out-of-plane, with clamping preventing any ferroelastic domain switching. Therefore, the film effectively behaves as a uniaxial ferroelectric.

The as-grown polarization of the film was out of plain and pointing up. In order to define a pattern of domains of opposite polarization direction, as shown in figure 6.4, domains were electrically switched by 180° using a Nanosensors PPP – EFM PtIr coated tip, with a k∼ 3 N/m, and applying a dc voltage of 3V to the tip.

Writing domains electrically can generate charge injection. In order to avoid electrostatic

---

[i] The sample was kindly provided by Dr. Eric Langenberg at Cornell University, USA.

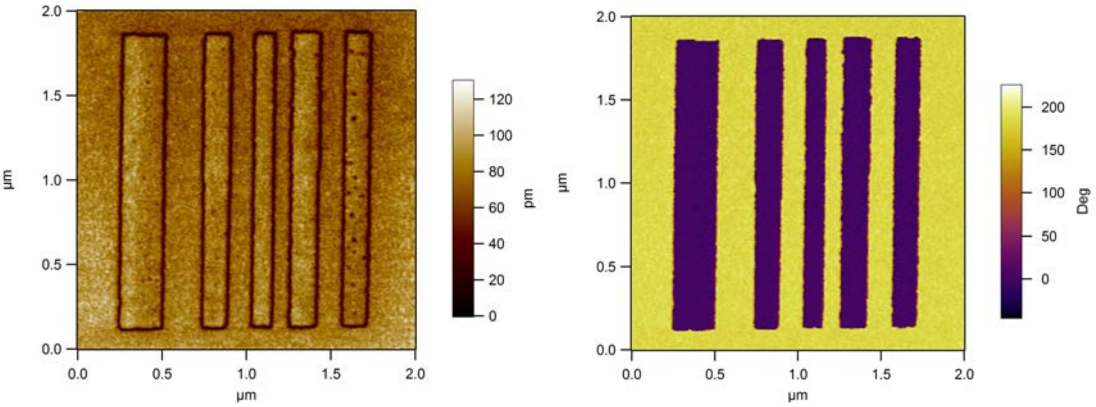

Figure 6.4: *PFM amplitude (a) and phase (b) of the electrically switched domains, with PhPFM = 0° for domains pointing down and PhPFM = 180° for domains pointing up.*

effects from these charges, and to ensure the stability of the written domains, CRF experiments were performed 36 hours after the switching of the domain. We used the same cantilever as for writing. The applied contact force was about 150 nN; this is a stronger load than for normal PFM reading (typically performed at few tens of nN), but not so strong as to induce undesired mechanical switching of polarization; mechanical writing typically happens in the hundreds of nN range. Figure 6.5 shows that, despite some relaxation around the edges, the written domain pattern is clearly visible both in the PFM phase image and, importantly, in the contact resonance frequency map. Downward oriented domains have a higher contact resonance frequency than the upward domains, in agreement with the nanoindentation and CRF results in the $LiNbO_3$ single crystals. It therefore appears to be a general feature of perovskite ferroelectrics: downward domains are stiffer than upward domains.

Interestingly, also, the resonance frequency contrast between domains is about one order of magnitude bigger for thin films (1 kHz) than equivalent measurements in single crystals (> 100Hz). The enhanced contrast is excellent news from the point of view of devices, since ferroelectric memories are thin film devices. We now turn our attention to the origin of the enhanced frequency contrast in thin films.

The analysis of this result should consider several aspects. First, the materials' intrinsic properties may differ between the two samples. For example, one may expect an enhanced

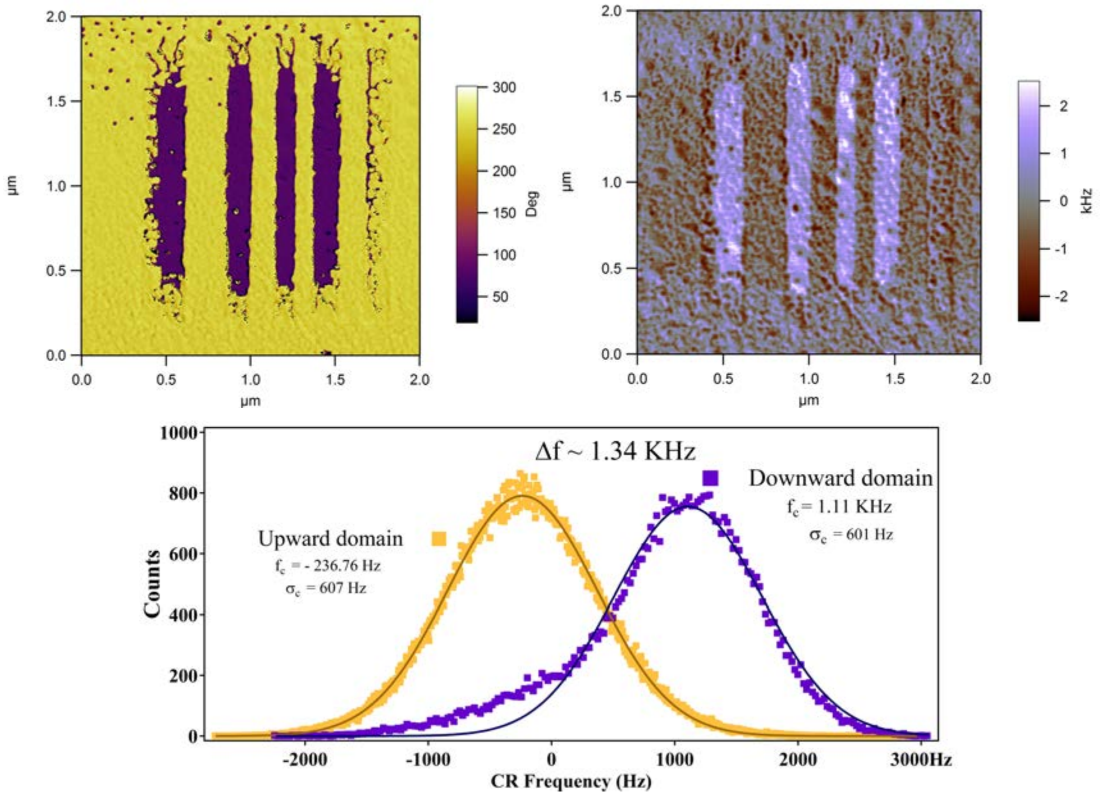

Figure 6.5: *(a)Phase PFM image showing the polarization of the switched domains in the $PbTiO_3$ sample, with PhPFM = 0º for domains pointing down and PhPFM = 180º for domains pointing up. (b). Contact resonance frequency mapping of the $PbTiO_3$ surface, the contact resonance frequency is shifted towards higher frequencies for down-polarized domains, meaning they are stiffer, and to lower frequencies for the up-polarized domains, meaning they are softer. (c). Histogram of the CR-AFM image shown in b: the yellow dots correspond to the frequency shift counts in the areas associated to domains pointing up and purple squares to domains pointing down. The lines are the corresponding Gaussian fittings, with parameters shown in the inset. The total CR frequency contrast among different polarized domains is of about $\Delta f \sim 1.1$ kHz, using a cantilever of $k \sim 3$ N/m.*

flexoelectric effect for $PbTiO_3$ as it has a higher dielectric constant as compared to $LiNbO_3$. However, the dielectric constant of monodomain PTO thin films is in fact almost the same as that of $LiNbO_3$ (both have relative permittivities around $\varepsilon_r = 30$). In fact, the flexocoupling coefficient determined from indentation for $LiNbO_3$ (see chapter 3) is of the order of a few tens of V, which is the same as the intrinsic flexocoupling coefficient measured for all other perovskite oxides, included some compositionally close to$PbTiO_3$such as $Pb(Mg,Nb)O_3 - PbTiO_3$. Differences between material constants are therefore small and unlikely to justify an enhancement of one order of magnitude in contact resonance frequency shift.

Instead, a more likely explanation for the enhanced contrast is an geometric size effect. The contrast in mechanical stiffness comes from the degree of competition between piezoelectricity and flexoelectricity. The strain gradient, however, is very localized within a region whose size is roughly proportional to the radius of the AFM tip. Thus, in a thin film, most of the sample directly under the tip is contributing to the flexoelectric signal, whereas in a single crystal only a tiny fraction of the volume is contributing. The competition between flexoelectricity and piezoelectricity should therefore be stronger in thin films. This size effect has been quantified theoretically. As calculated by Abdollahi et al.,[9] for the case of fracture toughness, the degree of asymmetry induced by flexoelectricity strongly depends on the normalized thickness of the material: they predict that, in $BaTiO_3$, the asymmetry goes from almost 0 for bulk sizes 100% for ultrathin epitaxial films with thicknesses of a few nm.

Perhaps a more inctuitive insight of the origin of the enhanced contrast is the consideration that, for PTO thin films, the pressure is below but close to the critical threshold for flexoelectric switching (as indicated earlier, this normally takes place in the hundreds of nN range). The induced flexoelectric fields are therefore strong enough to almost cancel the intrinsic ferroelectric polarization of the film for the domains in which both couple antiparallel, and, conversely, it should almost double the polarization in the domains where both couple parallel. This enormous flexoelectrically induced polar contrast of thin films must translate into an enhanced mechanical contrast as per the discussion in chapter 3. The more general conclusion is that, while size effects are generally detrimental in ferroelectrics, for flexoelectricity they can be helpful as they increase the relative strength of flexoelectricity (a size-dependent property) against piezoelectricity (a size-independent one), thereby enhancing the mechanical contrast that results form such competition. The size effects on the asymmetry of mechanical stiffness thus provide a tremendous advantage for mechanical reading of ferroelectric polarization in thin films.

All in all, the results shown in this chapter demonstrate the proof of concept of "mechanical read & write" of ferroelectric polarization; flexoelectricity not only offers a voltage-free way to mechanically "write" polarization, [4] but also to mechanically "read" it. Moreover, the mechanical reading of ferroelectric polarization in thin films benefits from the size effect in the asymmetry of mechanical properties that is predicted to scale with the decrease of structure sizes.

References

1. Abplanalp, M., Eng, L.M. & Günter, P. *Appl Phys A* **66**, S231-S234 (1998).
2. Eng, L.M., Abplanalp, M. & Günter, P. *Appl Phys A* **66**, S679-S683 (1998).
3. Rabe, U., Kopycinska, M., Hirsekorn, S., Muñoz-Saldaña, J., Schneider, G. A.& Arnold, W. J. *Phys. D: Appl. Phys.* **35**, 2621–2635 (2002).
4. Ocenásek, J., Lu, H., Bark, C. W., Eom, C. B., Alcalá, J., Catalan, G. & Gruverman, A. *Phys. Rev B* **92**, 035417 (2015).
5. Lu, H., Bark, C. –W., Esque de los Ojos, D., Alcalá, J., Eom, C. B., Catalán G. & A. Gruverman. *Science* **336**, 59 (2012).
6. Rabe, U., Amelio, S., Kester, E., Scherer, V., Hirsekorn, S. & Arnold, W. *Ultrasonics* **38**, 430-437 (2000).
7. Cordero-Edwards, K., Rodríguez, L. Calò, A., Esplandiu, M.J, Pérez-Dieste, V., Escudero, C., Domingo, N. & Verdaguer, A. *J. Phys. Chem. C* **42**, 120 (2016).
8. Rabe, U., Janser, K. & Arnold, W. *Rev. Sci. Instrum.* **67**, 3281-3293 (1996).
9. A. Abdollahi, C. Peco, D. Millán, M. Arroyo, G. Catalan & I. Arias. *Phys. Rev. B* **92**, 094101 (2015).

Part III

Conclusions

CHAPTER 7

Conclusions

This thesis is a contribution to the field of flexoelectricity. Its main novelty lies in the focus on the purely mechanical effects of flexoelectricity on ferroelectrics. Such mechanical focus is original compared to the more usual emphasis on electrical or electromechanical consequences. The key thesis is that the presence of strain gradients, and therefore flexoelectricity, when combined with ferroelectricity, breaks the symmetry in mechanical response, opening a new and interesting and unexplored field of study with a range of potentially useful functionalities. The main findings and conclusions of the present research can be summarized as follows:

- In both stoichiometric and congruent $LiNbO_3$, the space inversion symmetry in mechanical response is broken due to the flexoelectric effect. Thus the generally held assumption that the mechanical responses of crystals have to be symmetric because all the elastic tensors are also symmetric has been shown to be incorrect.

- The mechanical asymmetry of ferroelectrics implies that one can use external electrical stimuli to switch between two different types of mechanical response in ferroelectrics. For the cases of $LiNbO_3$ and $PbTiO_3$ (perovskite ferroelectrics), downward polarized material is stiffer but more brittle (high elastic constant, but low hardness) whereas upward-oriented domains are more elastic but also more robust against indentation.

- This switchable mechanical response may find uses in smart mechanical coatings with voltage-controlled mechanical properties. Based on this, we propose that, in addition to being considered as smart multifunctional materials, as it is done nowadays, ferroelectrics should also be considered as smart mechanical materials.

- The asymmetry in the mechanical response, together with the free energy of ferroelectrics, was used to explicitly calculate an analytical expression in order to extract the flexocoupling coefficient from mechanical nanoindentation measurements. The relative proximity of the value obtained to the theoretical value suggests that that this new method to estimate the flexocoupling coefficient is a reliable alternative to the classical electromechanical measurement methods based on measuring bending-induced polarization. For the specific case of ferroelectrics, in fact, purely mechanical measurements avoid spurious electrical contributions and thus yield a more accurate result.

- In an in-plane polarized uniaxial ferroelectric (Rb-doped KTP), it was shown that cracks propagate more easily parallel to the ferroelectric polarization than antiparallel to it. This is a direct consequence (and evidence) of fracture toughness being enhanced when flexoelectricity and ferroelectricity are antiparallel compared to when they are parallel. This kind of “crack diode” behaviour has implications for our understanding of fracture phenomena and mechanical fatigue in ferroelectrics; in particular, we speculate that microcracking-induced fatigue might be enhanced or mitigated depending on poling direction of the ferroelectric transducer.

- Finally, I was demonstrated that an AFM-based technique (Contact Resonance Frequency Microscopy, CRFM), is able to determine the polar sign of both single crystals and thin films by purely mechanical means, and thus without applying any voltage to the ferroelectric. Non-destructive mechanical reading of polarization represents a practical application of the asymmetry in the mechanical response, and opens up new device possibilities such as reading a ferroelectric memory without electrodes.